

A Quick-look Processor for Inverse Synthetic Aperture Radar (ISAR) Imaging of Sea Vessels



Prepared by:

Tristyn Ferreiro

FRRTRI001

Prepared for:

Dr. Yunus Abdul Gaffar

Department of Electrical Engineering

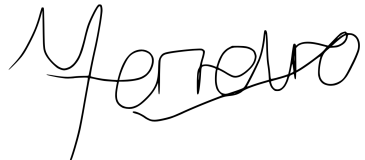
University of Cape Town

Submitted to the Department of Electrical Engineering at the University of Cape Town in partial fulfilment of the academic requirements for a Bachelor of Science degree in Electrical and Computer Engineering

October 31, 2023

Declaration

1. I know that plagiarism is wrong. Plagiarism is to use another's work and pretend that it is one's own.
2. I have used the IEEE convention for citation and referencing. Each contribution to, and quotation in, this report from the work(s) of other people has been attributed, and has been cited and referenced.
3. This report is my own work.
4. I have not allowed, and will not allow, anyone to copy my work with the intention of passing it off as their own work or part thereof.



October 31, 2023

Name Surname

Date

Acknowledgements

I would like to begin by expressing my gratitude to my supervisor, Dr. Yunus, who has consistently provided invaluable guidance and wisdom over the past few months. I appreciate your unwavering willingness to assist me, engage in meaningful discussions, and consistently go the extra mile to support me. Having you as a mentor has made this journey exceptionally fulfilling, and I am thankful for the knowledge and insights you've imparted. Your humility and kindness will continue to inspire me.

I would like to extend my appreciation to the Council for Scientific and Industrial Research (CSIR) for generously providing the measured data that were critical in this project's development.

To all of my friends, thank you for your love and support and your part in my journey. Ryan, thank you for believing in me when I failed and encouraging me when I felt defeated. Mishay, thank you for always being the voice of reason and rational thinking when everything felt overwhelming to me. Shams, your companionship throughout the last few years has provided me with many necessary moments of silliness and comfort. And to Justin Pead, thank you for being my mentor, for helping me solve many problems and providing me with endless oversized cups of tea to drown my stress in.

And, to my mom, who has been my biggest fan throughout my life. It's challenging to put into words just how much I value the sacrifices you've made and the support you've provided. The best I can offer is a heartfelt thank you, repeated over infinity times infinity.

Abstract

A Quick-look Processor for ISAR Imaging of Sea Vessels

Tristyn Ferreiro

Monday 30th October, 2023

This project investigates the use of low-computation Translational Motion Compensation (TMC) algorithms to enhance Inverse Synthetic Aperture Radar (ISAR) imaging of sea vessels. Recent advancements into high range resolution radar systems have enabled ISAR imaging for object classification. However, the non-cooperative motion of sea vessels often challenges the formation of focused ISAR images. The primary motivation for this research is the need for a tool to assess the quality of ISAR data collected during field experiments.

The project implemented two Range Alignment (RA) and two Autofocus (AF) algorithms, selected from the literature. The project focused on improving these algorithms' robustness and computational efficiency. Simulated and measured data was used to evaluate the performance of these algorithms on maritime data. Modifications were made to the AF algorithms to enhance their performance.

The best performing RA and AF algorithms were combined into a low-computation Quick-look Processor (QLP) for ISAR imaging. The final implemented QLP was a user-friendly MATLAB app. This QLP aimed to generate focused ISAR images efficiently, thus overcoming the traditional delay in data processing data recorded during field experiments.

Two case studies illustrated the QLP's robustness and its ability to assess data quality during field trials. The results confirm the project's objectives: the QLP effectively generated focused ISAR images in less time than the data measurement time. Additionally, the project bridged the research gap regarding low-computation RA and AF algorithms and QLPs in the context of sea vessel ISAR imaging.

Contents

List of Figures	viii
List of Tables	x
Abbreviations	xi
1 Introduction	1
1.1 Background	1
1.2 Problem Statement	2
1.3 Objectives	2
1.4 Technical Requirements	3
1.5 Scope & Limitations	3
1.6 Original Contributions	3
1.7 Report Outline	4
2 Theoretical Background	5
2.1 Radar Resolution Concepts in ISAR	5
2.1.1 Down-range Resolution	5
2.1.2 Doppler Frequency	5
2.1.3 Doppler Resolution	6
2.1.4 Range and Doppler Ambiguities	6
2.2 High Resolution Radar Waveforms	7
2.2.1 Background	7
2.2.2 Stepped Frequency Waveform (SFW)	7
2.2.3 High Resolution Range Profile (HRRP)	9
2.3 Inverse Synthetic Aperture Radar (ISAR) Range-Doppler Image Formation	10
2.3.1 Motion of Sea Vessels	10
2.4 Image Formation Pipeline	10
2.4.1 Motion Compensation	12
2.5 Translational Motion Compensation (TMC)	12
2.5.1 Range Alignment	12
2.5.2 Autofocus	13
2.6 Rotational Motion Compensation (RMC)	14
2.7 Important Concepts in ISAR	14
2.7.1 Noise	14
2.7.2 Coherent Processing Time Window Length (CPTWL)	14
2.7.3 Sidelobes	15

2.7.4	ISAR Image Contrast	15
3	Literature Review	16
3.1	Maritime Applications of ISAR	16
3.2	Complications in ISAR Imaging of Sea Vessels	17
3.2.1	Complex Motion	17
3.2.2	Focus vs Quality	18
3.3	Translation Motion Compensation	18
3.3.1	Range Alignment Algorithms	18
3.3.2	Autofocus Algorithms	19
3.4	Quick-look Processors in Radar	20
3.5	Critical Review	21
4	Algorithm Verification and Validation	22
4.1	ISAR Simulator	22
4.1.1	Simulator Changes	22
4.1.2	Description of Simulator Setup	22
4.2	Description of Measured Data Setup	24
4.3	Correlation Range Alignment Algorithm	26
4.3.1	Pseudo Code and Implementation	26
4.3.2	Algorithm Verification	27
4.3.3	Algorithm Validation	28
4.4	Haywood's Range Alignment Algorithm	29
4.4.1	Pseudo Code and Implementation	29
4.4.2	Algorithm Verification	29
4.4.3	Algorithm Validation	30
4.5	Single Dominant Scatterer Autofocus (SDSAF) Algorithm	31
4.5.1	Pseudo Code and Implementation	32
4.5.2	Algorithm Verification	32
4.5.3	Algorithm Validation	35
4.6	Multiple Dominant Scatterer Autofocus (MDSAF) Algorithm	38
4.6.1	Pseudo Code and Implementation	39
4.6.2	Algorithm Verification	40
4.6.3	Algorithm Validation	42
4.7	Optimisation of Implementation to Reduce Runtime	45
4.7.1	Correlation Range Alignment (RA) Algorithm	45
4.7.2	Haywood RA Algorithm	45
4.7.3	SDSAF Algorithm	45
4.7.4	MDSAF Algorithm	45
4.7.5	Runtime Testing	45
4.8	Summary	46
5	Quick-look Processor: Design	48
5.1	Technical Requirements	48

5.2	Measured Dataset	48
5.3	Design Implementation	49
5.3.1	Frame Extraction	49
5.3.2	Candidate Designs	49
5.4	Runtime Testing	50
5.4.1	Experimental Setup	50
5.4.2	Results and Discussion	50
5.5	Image Focus Testing	51
5.5.1	Experimental Setup	51
5.5.2	Results and Discussion	51
5.6	Summary of Findings	53
5.7	Final Design	54
5.7.1	App design	54
6	Quick-look Processor: Case Studies	57
6.1	Case Study 1: Impact of High Range Resolution (HRR) Profiles and Range Bins on QLP Runtime	57
6.1.1	Setup	57
6.1.2	Results and Discussion	58
6.2	Case Study 2: Using QLP to Visualise ISAR Images for Data Quality Assessment	58
6.2.1	Setup	59
6.2.2	Results and Discussion	59
7	Conclusions	62
7.1	Future Work	63
7.1.1	Algorithms	63
7.1.2	Quick-look Processor	63
Bibliography		65
A Repository		67
B Additional QLP Design Results		68
B.1	Image Contrast values of measured data frames	68
C Ethics Form		69

List of Figures

2.1	Doppler frequency relationship with radial velocity of object.	6
2.2	Transmitted Stepped Frequency Waveform (SFW)	8
2.3	Transmitted SFW burst train containing M bursts, each with N frequency-stepped pulses.	9
2.4	Two dimensional data matrix.	9
2.5	Block diagram showing the adapted ISAR image formation process used in this report.	11
2.6	Illustration of how object motion affects the focus of ISAR images.	11
2.7	Block diagram showing the RA part of the ISAR image formation process.	13
2.8	Block diagram showing the Autofocus (AF) part of the ISAR image formation process.	13
3.1	Optical and ISAR images of a Esperance yacht.	16
3.2	Optical and ISAR images of a bulk carrier ship to show how Coherent Processing Interval (CPI) affects focus of image.	17
4.1	Scatterer structure used for simulation based on boat features.	23
4.2	Simulated High Resolution Range Profile (HRRP)s and ISAR image for the object with 0 m/s translation motion and 6 deg/s rotation motion.	23
4.3	Simulated HRRPs and ISAR image for the object with 1 m/s translation motion and 6 deg/s rotation motion.	24
4.4	Optical image of Zay-Yaan KB6 fishing boat. Adapted from [1].	24
4.5	Different ISAR image frames produced from a single measured data set, before Translational Motion Compensation (TMC) was applied.	25
4.6	Range-aligned measured HRRPs: frame 1 (left) and 4 (right).	25
4.7	Simulated HRRPs before and after Correlation RA.	27
4.8	Simulated object with 0 m/s translation motion.	27
4.9	Staircase curve of range bin shifts per simulated HRRP for Correlation RA.	27
4.10	HRRPs of a measured data frame before and after Correlation RA.	28
4.11	Staircase curve of range bin shifts per measured HRRP for Correlation RA.	28
4.12	Simulated HRRPs before and after Haywood RA.	30
4.13	Simulated object with 0 m/s translation motion.	30
4.14	Linearised staircase curve of range bin shifts per simulated HRRP for Haywood RA. .	30
4.15	HRRPs of a measured data frame before and after Haywood RA.	31
4.16	Linearised staircase curve of range bin shifts per measured HRRP for Haywood RA. .	31
4.17	SDSAF Dominant Scatterer (DS) selection for Correlation range-aligned simulated HRRPs.	33
4.18	DS phase angle before and after SDSAF phase correction on simulated data.	33
4.19	ISAR image formed after SDSAF correction on Correlation range-aligned simulated HRRPs.	34
4.20	(a) Correlation range-aligned simulated ISAR image, (b) SDSAF autofocused simulated ISAR image, (c) ISAR image of simulated object with 0 m/s translation motion.	34

4.21 ISAR images formed using the original, Correlation range-aligned and SDSAF autofocused HRRPs of a single measured data frame.	35
4.22 Optical image of Zay-Yaan KB6 fishing boat. Adapted from [1].	35
4.23 Scatterer power for the selection of a DS in SDSAF applied to correlation range-aligned measured HRRPs.	36
4.24 Scatterer power for the selection of a DS in SDSAF using various threshold Scaling Factor for Haywood Autofocus (SF)s applied to Correlation range-aligned measured HRRPs.	37
4.25 ISAR images after SDSAF using different SFs applied to Correlation range-aligned measured HRRPs.	37
4.26 MDSAF DS selection for Correlation range-aligned simulated HRRPs.	40
4.27 Reference HRR profile selected for use in MDSAF using Correlation range-aligned simulated HRRPs.	41
4.28 First DS's phase angle before and after MDSAF phase correction.	41
4.29 (a) Correlation range-aligned ISAR image, (b) MDSAF autofocus ISAR image, (c) ISAR image of simulated object with 0 m/s translation motion.	41
4.30 Scatterer Amplitudes and object scatterers considered in MDSAF of Correlation range-aligned measured HRRPs.	43
4.31 MDSAF DS selection for Correlation range-aligned measured HRRPs before and after noise filtering.	43
4.32 Optical image of Zay-Yaan KB6 fishing boat. Adapted from [1].	44
4.33 ISAR images formed using the original, Correlation range-aligned and MDSAF autofocused HRRPs of a single measured data frame.	44
 5.1 Block diagram showing initial Quick-look Processor (QLP) design.	49
5.2 Different ISAR image frames produced from a single measured dataset, before TMC was applied.	51
5.3 ISAR images produced by each candidate design for frame 1 of the measured dataset. .	52
5.4 ISAR images produced by each candidate design for frame 2 of the measured dataset.	52
5.5 ISAR images produced by each candidate design for frame 3 of the measured dataset.	53
5.6 ISAR images produced by each candidate design for frame 4 of the measured dataset.	53
5.7 Block diagram showing the final QLP design.	54
5.8 Wireframe of QLP MATLAB app.	54
5.9 User flow diagram using the designed User Interface (UI) of the QLP MATLAB app. .	55
 6.1 Optical image of Zay-Yaan KB6 fishing boat. Adapted from [1].	60
6.2 Focused ISAR image frames produced by the QLP using dataset 1.	60
6.3 Focused ISAR image frames produced by the QLP using dataset 2.	61

List of Tables

4.1	SFW parameters for simulation.	23
4.2	Algorithm runtime optimisation timing results.	46
5.1	Technical requirements considered when designing the QLP.	48
5.2	SFW parameters of measured dataset used in QLP design.	48
5.3	Description of candidate QLP designs.	49
5.4	Effective runtimes of each candidate QLP design for a single measured dataset.	50
5.5	The Image Contrast (IC) improvement of the ISAR image produced by each candidate QLP design compared to the IC of the unfocused image for multiple frames of measured data.	51
5.6	Description of user interactions and QLP app flow.	56
6.1	Effective QLP runtimes for datasets that had different a number of HRRPs but the same number of range bins.	58
6.2	Effective QLP runtimes for datasets that had different a number of range bins but the same number of HRRPs.	58
6.3	SFW parameters of two different measured datasets.	59
B.1	The IC values of the ISAR image produced by each candidate QLP design for multiple frames of measured data.	68

Abbreviations

AF Autofocus

CLI Command-line Interface

CPI Coherent Processing Interval

CPTWL Coherent Processing Time Window Length

CSIR Council for Scientific and Industrial Research

DS Dominant Scatterer

DSA Dominant Scatterer Algorithm

FFT Fast Fourier Transform

HRR High Range Resolution

HRRP High Resolution Range Profile

IC Image Contrast

ISAR Inverse Synthetic Aperture Radar

JTF Joint Time-Frequency

MDSAF Multiple Dominant Scatterer Autofocus

PPP Prominent Point Processing

PRF Pulse Repetition Frequency

PRI Pulse Repetition Interval

QLP Quick-look Processor

RA Range Alignment

RCS Radar Cross Section

RLOS Radar Line of Sight

RMC Rotational Motion Compensation

SAR Synthetic Aperture Radar

SDSAF Single Dominant Scatterer Autofocus

SF Scaling Factor for Haywood Autofocus

SFW Stepped Frequency Waveform

SIR Signal-to-Interference Ratio

SNR Signal-to-Noise Ratio

TMC Translational Motion Compensation

UI User Interface

Chapter 1

Introduction

This report details the development of a **QLP** for **ISAR** imaging, specifically in the context of sea vessels. In this report, a **QLP** is a radar data processing tool that produces a motion compensated **ISAR** image from measured **HRR** profiles. It was developed for use in validating experiment setups in the field to ensure the collection of high-quality data. The project involved research into **ISAR** imaging and the implementation of low computation **ISAR** image processing algorithms. These algorithms were used in the design and implementation of a **QLP**, which was validated using multiple measured datasets.

1.1 Background

Radar images contain rich information that can be used for imaging and classification of objects [2]. In the past, sea vessels could not be classified because of their non-cooperative¹ motion and low range resolution radar systems. However, the introduction of **ISAR**, a radar imaging technique that does not require knowledge of the object's motion, and the development of radar systems with high range resolution capability has made imaging and classification of sea vessels possible. These advancements have had several applications in civilian wide-area persistent maritime surveillance [3].

HRR data can be used to produce a 2-D radar image of an object without a priori of the motion of the object. However, these images are often unfocused due to both the 3-D rotation and translation motion of the object. Sea vessels often exhibit both types of motion which vary drastically over time. This variability makes it challenging to achieve the necessary 2-D rotation motion required to generate an image that resembles the object. To compensate for the effects of translation motion, **RA** and **AF** algorithms can be used to produce focused images. Many **RA** and **AF** algorithms with varying levels of computational-complexity exist to focus the image [2, 4]. However, few have been comparatively analysed on the same datasets in the context of sea vessels.

ISAR imaging techniques and applications are an active area of research. As discussed in [5], **HRR** and high **Signal-to-Noise Ratio (SNR)** data is necessary for the continuation of this research. When collecting data for research, it is common practice to dedicate days to field work and only begin processing of the data in following months. **ISAR** data may be obtained using pulsed wave radar systems. These pulsed wave forms have several parameters that can be changed, which affect the quality² of the recorded data. Additionally, the systems are susceptible to noise and interference which

¹A term used to describe an object with unknown motion.

²Quality of data refers to various aspects such as range and cross-range resolution, wave frequencies that produce suitable backscatter intensity and whether the data is generally conducive to forming images that characterise the object

further affects the quality of the data [2]. However, until the data is processed, its quality cannot be assessed.

Importantly, a focused image is not the same as a good quality image of the object [6]. Although TMC may focus the image, if the quality of the data collected is not suitable, an image containing clear object characterisation will not be produced. As discussed before, the collected data is affected by equipment setup and other conditions.

In other research areas such as detection of small sea vessels [5] and pulse-compression processing [7], low-complexity and low-computation QLPs have been built to aid in assessing the quality of data collected in the field. These processors are used to provide feedback on equipment setup during field work to ensure the collection of high quality data. The low-computation aspect removes the need for expensive, specialised, and high processing power machines to be used in the field.

1.2 Problem Statement

ISAR image processing is a specialised technique that requires HRR data to produce a 2-D image of an object [2]. The object's translation motion complicates the imaging process and is compensated by using RA and AF techniques. Considerable research into motion compensation techniques and other ISAR applications exists, but the progression of this research depends on the availability of high-quality data. Days are dedicated to collect ISAR data [1], however, the data quality can only be assessed in the months following data collection.

Whilst research has been conducted on different TMC techniques, there is insufficient work in the literature on comparing the performance of different RA and AF algorithms on the same dataset. Additionally, it was revealed that there is insufficient work on the performance of low computation algorithms, specifically in the context of maritime data.

The problem addressed in this project was using low computation RA and AF algorithms to produce well-focused ISAR images of sea vessels. This can be used by researchers to assess data quality in the field and, thereby, identify potential issues with the experimental setup.

1.3 Objectives

The broad objective of this project was to design a QLP for ISAR imaging of sea vessels. The following list outlines the objectives

- Select and implement low-computation TMC techniques to focus the ISAR images. Verify and validate the implementation of these techniques before use in the QLP. Improve robustness and runtime where possible.
- Investigate and compare the performance of different combinations of the implemented algorithms. Select the best performing RA and AF algorithm for use in the QLP. In the selection step, assess both the computational speed and quality of the focused image.

features.

- Develop a **QLP** that uses **HRR** profiles and **TMC** algorithms to produce a video containing focused **ISAR** images and that is suitable for use in the field.

1.4 Technical Requirements

Based on the objectives of the project discussed in [section 1.3](#), the following technical requirements were defined

- The **QLP** should process the data in a shorter time than the measurement time of the data.
- The **QLP** should produce a more focused **ISAR** image after **TMC**.
- The **QLP** should be user-friendly.

1.5 Scope & Limitations

The time available to complete the project was approximately 13 weeks which prevented thorough research into all aspects of the problem.

The scope of the project involved implementing two **RA** and two **AF** low computation algorithms in MATLAB. Followed by verification and validation of these algorithms as well as improvements to the robustness and the processing time of each algorithm. These algorithms were candidate algorithms for the **QLP**. Each candidate algorithm was validated in terms of image quality and processing time. Thereafter, the best **RA** and **AF** combination was selected for the **QLP**. Next, the **QLP** was applied to a few measured datasets of sea vessels.

There were several project limitations. First, only non-parametric **TMC** was investigated. Additionally, only **RA** and **AF TMC** algorithms were considered and, no **Rotational Motion Compensation (RMC)** or other processes were investigated or implemented to attempt to focus the **ISAR** image. No new radar data was collected during the project, rather measured datasets from the **Council for Scientific and Industrial Research (CSIR)** were used. MATLAB was selected as the software platform for this project due to its efficient matrix operation features. The effect of **CPI** on the focus of the images was not discussed or investigated, and the **CPI** value was kept constant throughout the report. Finally, the scope of the project was limited to radar datasets of sea vessels measured using a **SFW**.

1.6 Original Contributions

During the implementation of the algorithms considered in this report, various adjustments were made to enhance both their robustness and quality of the **ISAR** images generated. These adjustments include:

- For **SDSAF**, a technique for selecting a higher power **DS** was introduced to improve the focus of the images.
- For **MDSAF**, several modifications were made to [8]’s algorithm to improve the focus of the images. A noise filtering technique was introduced to ensure that the algorithm only selected scatterers within the object to focus the image. Additionally, [8] suggested using 6-18 scatterers,

but it was determined that this range was not always feasible. Consequently, the highest number below eleven was chosen. Finally, [8] did not specify how to select the reference profile used in focusing the image, a technique was introduced for systematically selecting the profile.

Additionally, the literature survey revealed that while research on QLPs has been conducted for other radar applications [5, 9], there is limited research pertaining to QLPs for ISAR imaging of sea vessels. This report presents the design and implementation of a low-complexity QLP to address this research gap.

1.7 Report Outline

The report begins with a theoretical background to develop ISAR imaging concepts in Chapter 2. Thereafter, a broad review of literature relevant to this project in Chapter 3. Chapter 4 then describes the verification and validation of the RA and AF algorithms implemented in this report. These algorithms are considered and evaluated for use in the QLP system design discussed in Chapter 5. Thereafter, the QLP is tested on different measured datasets in Chapter 6. Finally, Chapter 7 provides the conclusions drawn and is followed by recommendations for future work. Appendices provide additional results for sections throughout the report.

Chapter 2

Theoretical Background

This chapter provides the theoretical foundation for ISAR imaging concepts used throughout this report. General radar principles in the context of ISAR are discussed. Thereafter, the waveform¹ used in the simulated and measured data in this report is discussed. A brief description of the motion seen in sea vessels was provided. Thereafter, ISAR image formation was explained. Finally, an explanation of other important concepts in ISAR was provided.

2.1 Radar Resolution Concepts in ISAR

Radar resolution defines a radar's ability to resolve objects or scatterers closely spaced in terms of range, angle, or Doppler frequency. If the objects are closer spaced than the radar's resolution, they cannot be reliably resolved [10]. The resolution requirements of radar systems vary depending on their specific application. For example, ISAR imaging employs high-resolution radar to form detailed images.

2.1.1 Down-range Resolution

An object's range, R , is determined by measuring the round-trip time delay of the transmitted signal and its echoed return. In general, the range resolution of a radar describes its ability to resolve closely spaced objects in range. In ISAR imaging this concept is known as the down-range resolution and describes the ability to resolve individual scatterers on the object [2]. The range resolution is inversely proportional to the bandwidth of the radar system, mathematically, this relationship is approximated as

$$\Delta R = \frac{c}{2BW} \quad (2.1)$$

where ΔR is the range resolution, BW is the bandwidth and c is the speed of light constant [10].

2.1.2 Doppler Frequency

If there is relative motion between the radar and an object, the frequency of the returned signal will differ from the frequency of the transmitted signal. This is known as the Doppler effect and the difference in frequency is the Doppler frequency, f_D . Doppler frequency is valuable in ISAR image formation. This is because object scatterers have different speeds, resulting in distinct changes in Doppler frequency, which can be used to calculate the spacing between points [11]. A thorough explanation of this concept is given in Chapter 2 and 8 of [10]. In a mono-static radar system the

¹The term waveform refers to the signal generated and transmitted by the radar. The term signal refers to the radiated object's response to the waveform. However they are used interchangeably in this chapter

2.1. Radar Resolution Concepts in ISAR

Doppler frequency can be mathematically described in terms of the radial velocity of the object as

$$f_D = \pm \frac{2v}{\lambda} \cos \beta \quad \lambda = \frac{f_{transmit}}{c} \quad (2.2)$$

where λ is the wavelength of the transmitted signal, β the angle between the velocity vector of the object and the [Radar Line of Sight \(RLOS\)](#) and $v \cos \beta$ is the radial velocity. Radial velocity is the relative velocity between the radar and the object along the [RLOS](#). Figure 2.1 is an illustration to aid understanding of the concepts and terms discussed in this section.

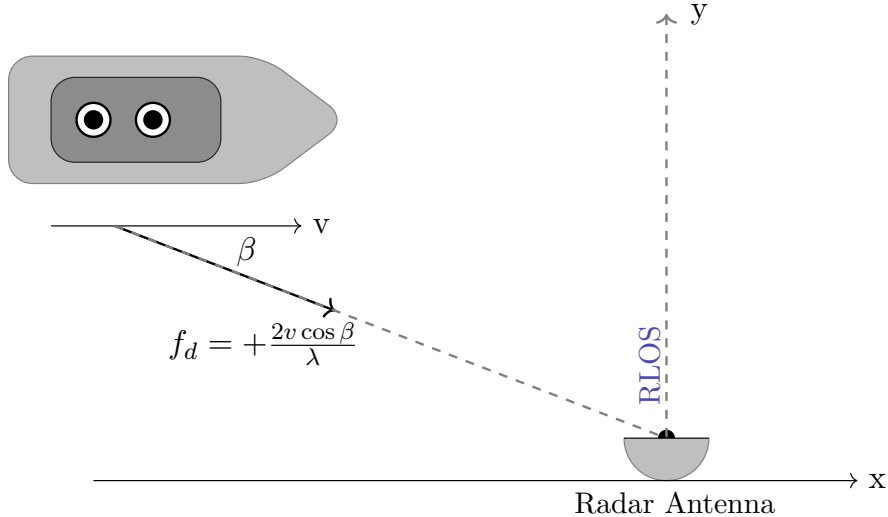


Figure 2.1: Doppler frequency relationship with radial velocity of object.

2.1.3 Doppler Resolution

Doppler resolution refers to the smallest separation between objects in terms of Doppler frequency, f_D , that the radar can resolve [10]. The relationship between Doppler resolution and the radar's dwell time, T_d , is given as

$$\Delta f_D = \frac{1}{T_d} \quad (2.3)$$

Chapter 8.4.7 of [10] provides a thorough explanation of the relationship.

2.1.4 Range and Doppler Ambiguities

The maximum range between the radar and object that can be unambiguously measured is given by

$$R_u = \frac{c}{2 \cdot PRF} \quad (2.4)$$

where c is the speed of light constant [10]. The Doppler frequency range that can be unambiguously measured is defined in [10] as

$$f_{D_u} = \pm \frac{PRF}{2} \quad (2.5)$$

There is a clear trade-off between the ambiguity of the range and Doppler frequency measurements. Increasing the [Pulse Repetition Frequency \(PRF\)](#) improves the unambiguous Doppler frequency but

decreases the unambiguous radar range. This trade-off and its effect on radar systems is thoroughly discussed in [10].

2.2 High Resolution Radar Waveforms

This section provides an in-depth explanation of the waveform used by the CSIR to collect the measured data used in this report. Although no raw radar data was collected in this report, an existing simulator that uses the same form was adapted for use in this report. To understand how the simulator was built and how it was able to generate HRRPs, an understanding of SFW was required. Additionally, explanations of the waveform in the literature was found to be difficult to understand, this section aimed to simplify the main concepts.

2.2.1 Background

Low resolution radar systems cannot resolve scatterers of an object when the object's size is less than the radar's range resolution. In contrast, high resolution radar systems can resolve individual scatterers² on an object. To achieve high range resolution, these systems employ waveforms with varying interpulse frequencies that create a wide effective bandwidth [10]. Frequency modulation of signals is used to achieve the varying interpulse frequencies. Chirp pulse³, phase-coded waveforms and pulsed SFW exist for this purpose [2].

2.2.2 Stepped Frequency Waveform (SFW)

SFW signals are discussed in detail in [2, 4, 12], this section highlights the core concepts. A SFW waveform, shown in Figure 2.2, is illustrated as a series of pulses with increasing carrier frequencies of fixed increments.

Mathematically, the carrier frequency of each pulse can be expressed as

$$f_n = f_0 + (n - 1) \cdot \Delta f \quad (n = 1, \dots, N) \quad (2.6)$$

where f_0 is the frequency of the first pulse, n is the pulse number, N is the total number of pulses in the waveform and Δf is the frequency step [2].

The interpulse frequency modulation results in a wide effective bandwidth

$$BW_{eff} = N \cdot \Delta f \quad (2.7)$$

Wehner [12] derives the unambiguous range of this waveform as

$$R_{ua} = \frac{c}{2\Delta f} \quad (2.8)$$

²When a radar transmits an electromagnetic wave at an object, that object reflects or scatters the wave. As discussed by Wehner [12], an object is made up of individual reflection points called scatterers or scattering centers. More about these concepts can be found in [10, 12]

³Also known as a linear frequency modulated pulsed waveform

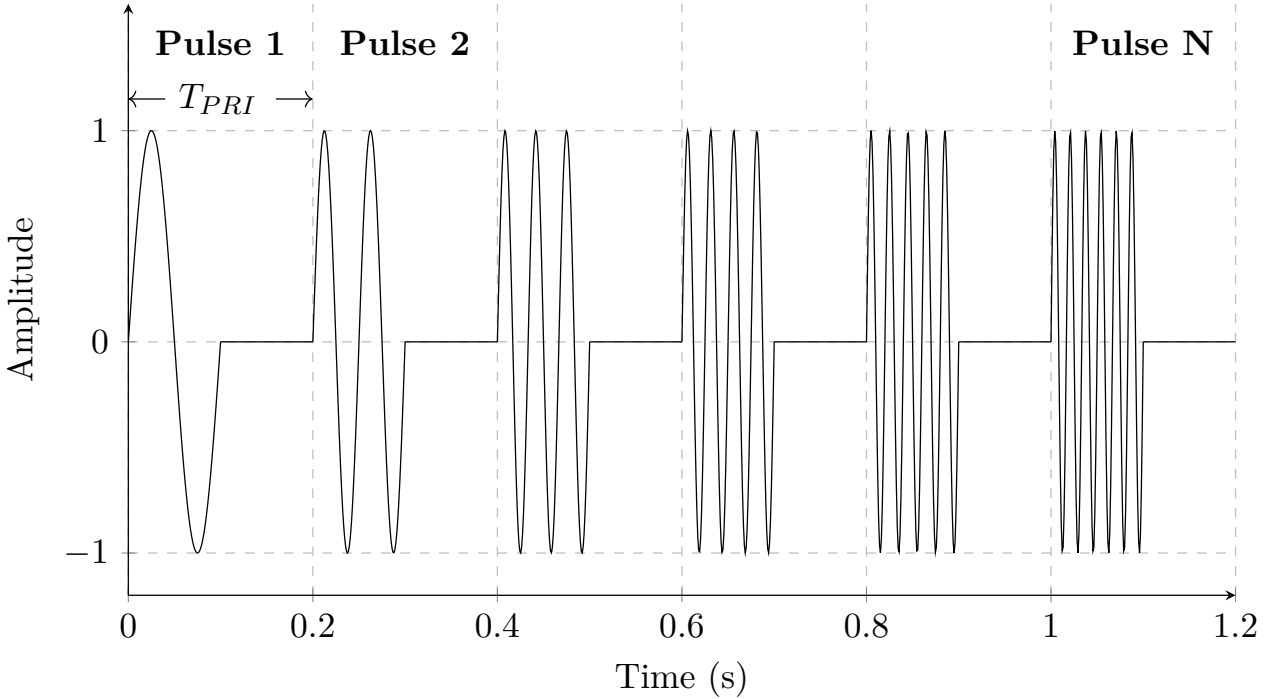


Figure 2.2: Transmitted SFW

and the range resolution in [Equation 2.1](#), is redefined in terms of the effective bandwidth as

$$\Delta R = \frac{c}{2 \cdot N \cdot \Delta f} \quad (2.9)$$

By increasing the number of pulses, size of the frequency step or both, a wider effective bandwidth can be achieved. The wide bandwidth capability of [SFW](#) is advantageous for high resolution radar applications like [ISAR](#).

In practice, the radar transmits a sequence of [SFW](#) signals as illustrated in [Figure 2.3](#). Each sequence consists of M [SFW](#) signals, referred to as bursts, with each burst containing N frequency-stepped pulses [\[2\]](#). As indicated in [Figure 2.3](#) the burst repetition interval is

$$T_{burstInterval} = N \cdot T_{PulseRepetitionInterval(PRI)} \quad (2.10)$$

where N is the number of pulses in the burst and T_{PRI} is the [SFW](#) signal's [PRI](#). The dwell time per burst is $T_d = N \cdot T_{PRI}$ [\[10\]](#) and the Doppler resolution given in [Equation 2.3](#) can be redefined as

$$\Delta f_D = \frac{1}{N \cdot T_{PRI}} \quad (2.11)$$

The total [CPI](#) of a [SFW](#) radar is dependent on the number of bursts and is defined by [\[4\]](#) as

$$T_{CPI} = M \cdot T_{burst} = M \cdot N \cdot T_{PRI} \quad (2.12)$$

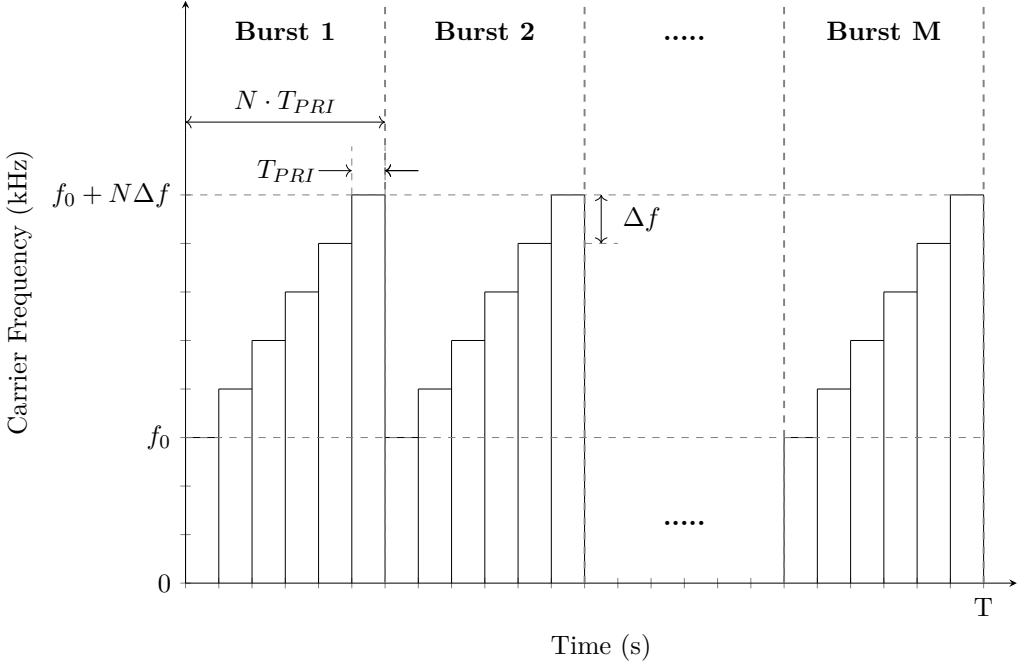


Figure 2.3: Transmitted [SFW](#) burst train containing M bursts, each with N frequency-stepped pulses.

2.2.3 High Resolution Range Profile ([HRRP](#))

Synthetic range profiles can be generated using [SFW](#) signals, this process is detailed in [12]. A [HRRP](#) is a 1-D projection of the objects returns onto the [RLOS](#) which shows the down-range separation of object scatterers. The process of generating [HRRPs](#) using [SFW](#) as well as the benefits and challenges are detailed in [12]. The key idea is that the return from a single [SFW](#) burst is a single [HRRP](#). The number of pulses, N , in the burst determines the number of range bins in the [HRRP](#). In [Figure 2.4](#), each row is a [HRRP](#) consisting of N range bins.

When M successive bursts are fired, as illustrated by the burst train in [Figure 2.3](#), M [HRRPs](#) are formed [2]. These [HRRPs](#) are stacked together to form the data-matrix illustrated in [Figure 2.4](#).

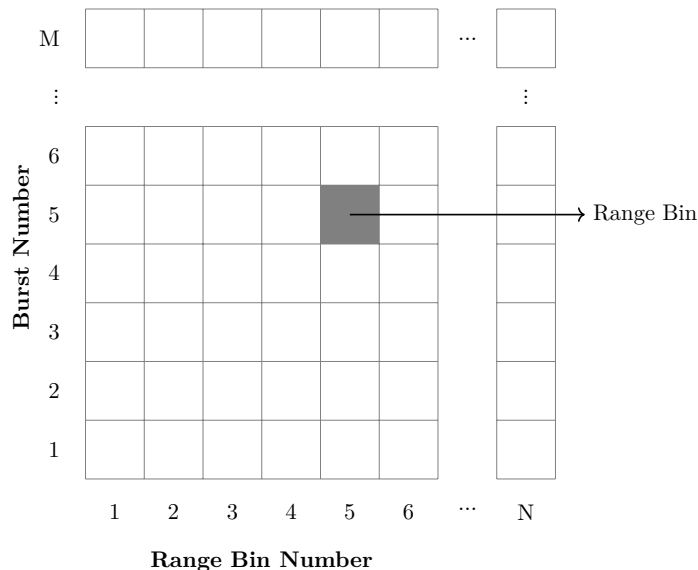


Figure 2.4: Two dimensional data matrix.

2.3 ISAR Range-Doppler Image Formation

To form an **ISAR** image, the object must be in motion with respect to the radar in such a way that there are different look angles over the **CPI** [4]. This data is used to form the 2-D range-Doppler **ISAR** image. It is the object's rotation motion that gives rise to scatterers in cross-range with different Doppler frequencies. However, in reality, objects exhibit undesired motion which results in Doppler shifting that negatively impacts the image.

2.3.1 Motion of Sea Vessels

In ISAR imaging, rotation motion of the object is required to form the image. As thoroughly presented in Chapter 6 of [2], a small rotation of the object with respect to the **RLOS** is adequate to form the range-Doppler **ISAR** image.

There are two types of objects: cooperative and non-cooperative [11]. Cooperative objects are those with a priori motion parameters and are easier to image. Imaging of non-cooperative targets is one of the main advantages of **ISAR** imaging over other radar imaging techniques. Sea vessels are an example of non-cooperative objects. Their motion is not only affected by their own motion but also external factors such as waves [6]. The effects of these external factors on the object's motion is unknown unless in-situ sensors are available to record such information.

Furthermore, sea vessels exhibit complex 3-D motion in both rotation and translation. The rotation motion is often referred to as yaw, pitch and roll [3]. This complex motion leads to unfocused **ISAR** images since the axis of rotation is not fixed over the **CPI**.

In the case of small sea vessels, their complex 3-D motion often varies drastically over the **CPI** which results in further degradation of the image [8]. **ISAR** datasets contain many **HRRPs** which can be subsetted to reduce the **CPI**, as discussed in subsection 2.7.2. Reducing the **CPI** aims to find an optimal time window where the object's motion is relatively constant - thus meeting the condition for well-focused **ISAR** images [6]. The effects of **CPI** on the focus of the image is out of the scope of the project, but has been included in this chapter and chapter 3 for completeness. The **CPI** is kept small but constant throughout this report.

2.4 Image Formation Pipeline

The general approach to forming an **ISAR** range-Doppler image involves several steps, namely match filtering, **TMC**, **RMC**, and **Fast Fourier Transform (FFT)** or **Joint Time-Frequency (JTF)** processing. In this report, the image formation process is adapted for the specific **QLP** use-case. Specifically, pre-constructed **HRRP** data is used and only **TMC** techniques will be implemented, as illustrated in Figure 2.5. For readers looking to understand the complete process, [2, 4, 3] are recommended.

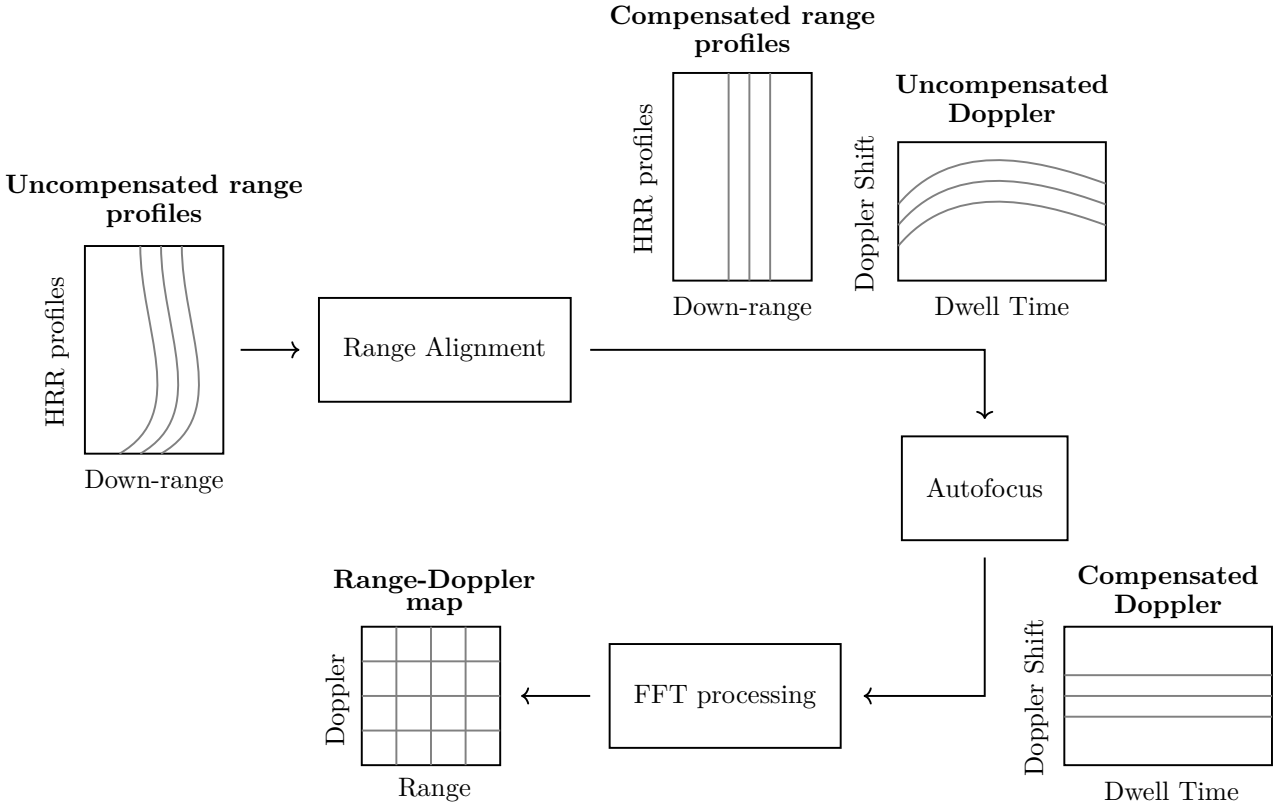


Figure 2.5: Block diagram showing the adapted ISAR image formation process used in this report.

Due to the motion of an object, it can appear at different positions across range profiles [2]. This motion can be categorised into translation and rotation motion. Motion compensation is an important step in forming focused ISAR images. The goal of this step is to reduce the smearing effect that an object's motion has on the image. Figure 2.6 illustrates how an object's uncompensated motion affects the focus of the image. In Figure 2.6b, the scatterers are spread over both the range and Doppler axes and are not clearly distinguishable. The spread can be seen by the increase in height and width of the scatterers in Figure 2.6b relative to those in Figure 2.6a

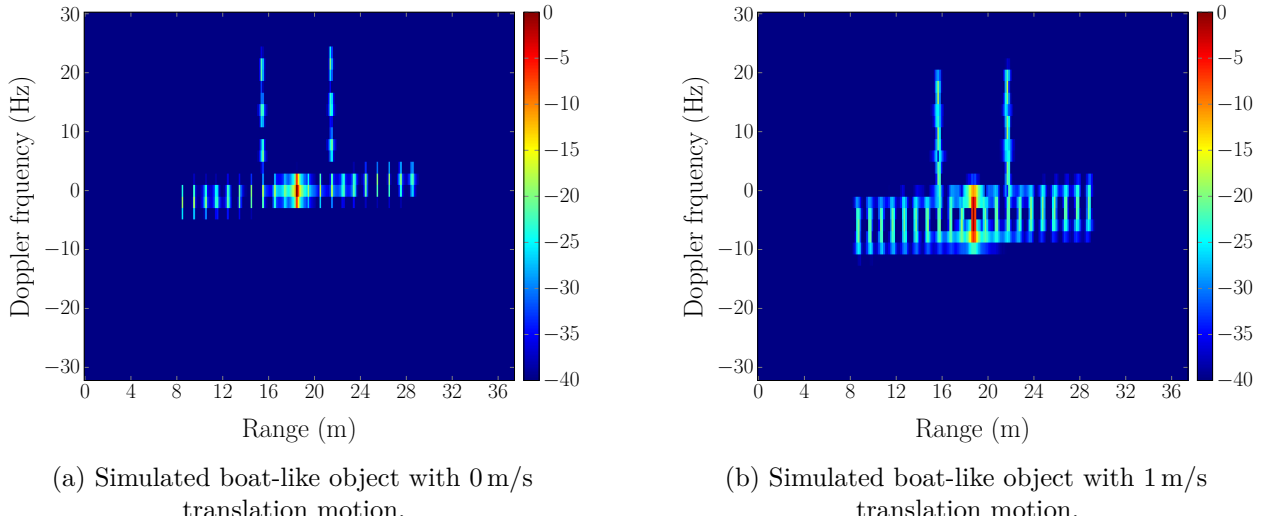


Figure 2.6: Illustration of how object motion affects the focus of ISAR images.

2.4.1 Motion Compensation

Pure small rotation motion which is required to form a well-focused **ISAR** image, does not occur in measured data [6]. Instead, objects exhibit complex 3-D translation and rotation motion. To compensate for this, **TMC** and **RMC** are used to form focused **ISAR** images. Motion compensation removes or reduces the effects of an object's translation or large rotation motion to achieve a pure small rotational motion needed to construct the **ISAR** image [2].

Effective motion compensation ensures that the energy of scatterers in each range bin is accurately separated according to their respective Doppler frequencies ???. As a result, a well-focused **ISAR** image is generated.

In this report, only **TMC** techniques are investigated and implemented, which will be the focus of subsequent sections. Nonetheless, for the sake of completeness, contextual information regarding **RMC** is provided.

2.5 Translational Motion Compensation (TMC)

Two categories of **TMC** techniques exist [11]: parametric and non-parametric algorithms. Parametric algorithms require knowledge of the object's motion, amongst other parameters, to perform motion compensation. However, in the context of non-cooperative objects, such as sea vessels, these parameters are not known. In these cases, non-parametric techniques are used. Non-parametric algorithms, which are the focus of this report, use two steps to compensate the object's motion: **RA** and **AF**.

2.5.1 Range Alignment

RA compensates the object's translation motion by aligning all scatterers such that they remain in one range bin over the duration of the **CPI** [11, 2].

Figure 2.7 illustrates this process. The block labeled 1 simplistically demonstrates uncompensated **HRRPs**. It shows 3 scatterers that, due to the object's translation motion, move between **HRRPs**. Due to this movement, no straight line scatterers are observed. After **RA** is applied, the block labeled 2 shows that range aligned profiles are produced. The 3 scatterers are now observed as straight lines, which illustrates that they remain in the same range bin over the duration of the **CPI**. Additionally, the block labeled 3 demonstrates that after **RA**, the phase of scatterers is non-uniform and needs to be compensated.

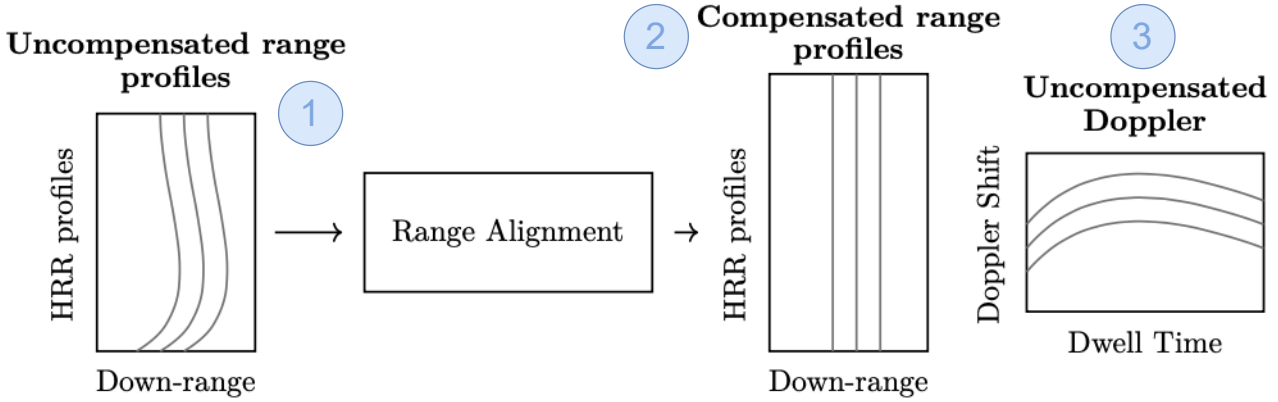


Figure 2.7: Block diagram showing the RA part of the ISAR image formation process.

If the phase errors introduced by RA are not compensated, the ISAR image will exhibit Doppler spreading which causes defocusing [2].

2.5.2 Autofocus

AF applies phase correction to the HRRPs to remove, or if not possible, reduce the varying phase angle of the scatterers over the CPI [2]. If not compensated, these phase errors will result in unfocused ISAR images.

Figure 2.8 illustrates the ideal outcome of the AF process. The block labeled 1 demonstrates that the three scatterers exhibit varying phases over the duration of the CPI. It is this effect that results in defocused ISAR images where scatterers are smeared over the Doppler axis. After phase compensation, straight lines are seen in block 2. This illustrates that the varying phase has been corrected such that the scatterers exhibit uniform phase over the CPI.

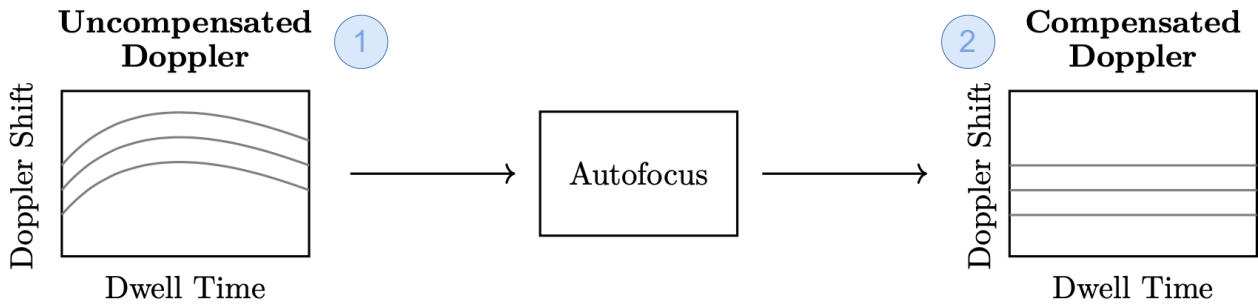


Figure 2.8: Block diagram showing the AF part of the ISAR image formation process.

The result shown in Figure 2.8 is an ideal case and is not always attainable. However, if complete compensation is achieved, a well-focused ISAR image will be formed.

2.6 Rotational Motion Compensation (RMC)

Generally, this step is carried out after applying the [TMC](#) because it has a smaller impact on the image's focus [4]. It is important to remember that a slight rotation of the object in relation to the [RLOS](#) is required to generate the range-Doppler image. However, if the object undergoes significant rotation during the [CPI](#), the image may remain unfocused even after applying [TMC](#). In such instances, the object's large rotation motion causes a time-varying Doppler frequency shift. This drifting cannot be compensated for by [TMC](#) since it is influenced by the object's angular rotation rate, Ω . Large rotation motion is frequently observed in objects like aircraft or sea vessels in rough sea conditions, which are not the primary focus of investigation in this report. For further insights into the challenges posed by large object rotation and [RMC](#) techniques, refer to [2, 4].

2.7 Important Concepts in ISAR

2.7.1 Noise

The [SNR](#) represents the ratio of the received signal power, P_r , to the noise power, P_n . This noise power is usually considered to be the effect of the radar receiver's thermal noise [10]. However, signal interference in radar systems can result from various sources beyond receiver thermal noise [10]. The [Signal-to-Interference Ratio \(SIR\)](#) takes all interference sources into account and is determined by the ratio of P_r to the total interference. It is given in [10] as

$$SIR = \frac{P_r}{N + C + J} \quad (2.13)$$

where N is the receiver thermal noise, C is clutter, and J is jamming noise. This equation does not include all possible interference sources, but rather shows that P_n is the sum of multiple interference factors. The [SIR](#) is what determines the radar performance, although it is often simplified to [SNR](#).

Interference not only impacts the power of the received signal but also its phase. As discussed in [subsection 2.1.2](#), the Doppler shift is determined using the phase of the received signal. Any sources of interference can introduce phase modulation to the signal, consequently affecting the accuracy of calculated Doppler shifts. The influence of various interference sources on the received signal is discussed in Chapter 12.2 and throughout [10]. A critical consideration for this report is that phase noise leads to Doppler spectral spreading. In the context of [SFW](#) and synthetic aperture systems, it can also result in increased sidelobes during image processing, consequently distorting the image in an undesirable manner.

2.7.2 CPTWL

An object's complex motion impacts the focus of an [ISAR](#) image relative to the [CPTWL](#). The [CPTWL](#) is given in [2] as

$$CPTWL = CPI \cdot PRF \quad (2.14)$$

where [CPI](#) is the number of [HRRPs](#) and [PRF](#) is the repetition frequency of the bursts in a [SFW](#) used to form the profiles.

As previously discussed in this chapter, a well focused ISAR image is formed when an object has a constant rotation over time. However, in the case of sea vessels, where nonuniform pitching, yawing and rolling is often observed, the effective rotation of the object changes over time. Subsequently, as discussed in Chapter 6 of [2], this leads to severe defocusing of the ISAR image.

Since ISAR imaging is often used in the context of non-cooperative object's, it is not possible to know the optimal time window to produce a well focused image a priori. Therefore, data is collected over a long period of time and is then processed to extract a few well-focused ISAR images. During processing, the CPI is reduced to a smaller number of HRRPs in an attempt to find a time window where the object's motion is relatively constant.

2.7.3 Sidelobes

Generally in frequency modulated waveforms, high sidelobes appear adjacent to or near the mainlobe, and decrease with distance from the mainlobe [10]. The high peak sidelobes are a result of the spectrum's sharp transition in frequency between pulses.

Noise, specifically that affects the phase, can lead to large signal sidelobes which results in Doppler spreading. When large sidelobes appear in ISAR data they distort the image which appears as the spreading of scatterers across the Doppler spectrum. Specifically, after AF, the power of a scatterer will remain in its range bin but be spread over the Doppler axis.

Different filters exist to reduce the effects of sidelobes, as discussed in Chapter 3.3 of [2]. One such filter is a simple Hamming window which was applied to the images in this report. However, more advanced and effective filters exist. The disadvantage of applying these filters is a reduction in SNR and a subsequent loss in resolution [10].

2.7.4 ISAR Image Contrast

As discussed in [13], IC can be used to measure the focus of an image. The idea behind this is that in a focused image, the power of object scatterers is less spread and so become more pronounced than in an unfocused image. The IC is calculated using the intensity and mean power of the image:

$$IC = \frac{\sqrt{(I - A\{I\})^2}}{A\{I\}} \quad (2.15)$$

Where I is the intensity of all range bins in the image calculated as $|amplitude|^2$ and A is the mean function.

This calculation is sensitive to anomalies in the data which may result in incorrect quantification of the performance of the TMC techniques in focusing the image [11].

Chapter 3

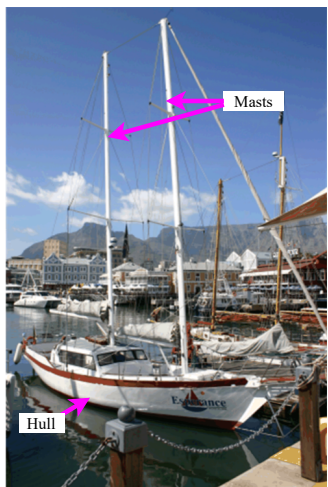
Literature Review

This chapter establishes the context for this project by surveying existing literature. [3, 6] revealed that **ISAR** imaging has been an active area of research for decades and has several applications. This literature review focuses on **ISAR** imaging of sea vessels.

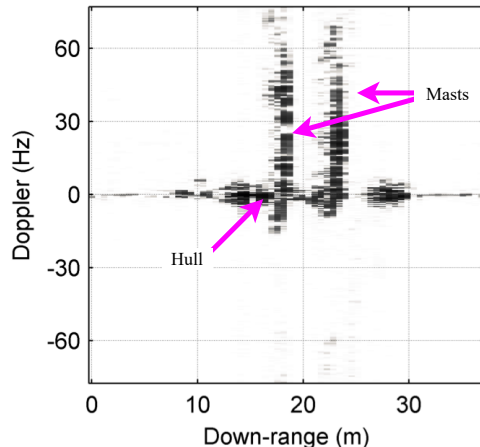
It begins by exploring the use of **ISAR** in maritime applications. Thereafter, **TMC** techniques for focusing of **ISAR** images are discussed. The chapter then provides an analysis of literature which discusses the use of **QLPs** in assessing the quality of data collected during field work. The review concludes with a critique of the literature to summarise critical information for this report.

3.1 Maritime Applications of **ISAR**

Radar images contain rich information that can be used for imaging and classification of objects [2]. In the past, sea vessels could not be classified because of their non-cooperative motion and low range resolution radar systems. However, the introduction of **ISAR**, a radar imaging technique that does not require knowledge of the object's motion, and the development of radar systems with high range resolution capability has made imaging and classification of sea vessels possible. These advancements have made **ISAR** desirable for several military and civilian applications [3].



(a) Optical image. Adapted from [3].



(b) **ISAR** image. Adapted from [3].

Figure 3.1: Optical and **ISAR** images of a Esperance yacht.

The rich information contained in ISAR images can be used for feature extraction which is used for object classification [6]. An example of how ISAR images can be seen to show object features is illustrated in Figure 3.1. In maritime applications, ISAR images prove useful for extracting features of all types of sea vessels [14]. Classification of sea vessels is used in civilian maritime surveillance to protect against activities such as organised crime and illegal fishing [15].

Additionally, naval sea vessels need to have a low Radar Cross Section (RCS) to minimise the likelihood of them being detected by radar systems [3]. ISAR images illustrate the RCS of objects well. Therefore, ISAR images can be used to aid RCS management in military maritime applications.

3.2 Complications in ISAR Imaging of Sea Vessels

Generating ISAR images of sea vessels proves to be a complicated problem. There are parameters that affect the focus and quality of the image.

3.2.1 Complex Motion

[6, 3, 2] showed that the primary drawback of using ISAR for imaging is that obtaining good images is not always achievable. As discussed in [2], to acquire a well-focused ISAR image, the object must maintain time-invariant angular motion relative to the radar throughout the duration of the CPI. However, for the imaging of sea vessels, achieving this level of motion stability is often impossible. Consequently, well-focused images of sea vessels, although valuable for classification purposes, are not consistently obtainable [6].

The challenge arises from their complex non-cooperative motion, which, as discussed in [3], impacts the focus of the generated images. Before well-focused images can be formed, compensation for the object's translation motion is required [2]. There are many TMC algorithms developed for this purpose, some of which are discussed in section 3.3. In [8], it was observed that the smaller the boat, the more its motion varies over time. Due to the high variability in the motion of small boats throughout the CPI, relying solely on TMC proves inadequate in producing focused images of small sea vessels [8].

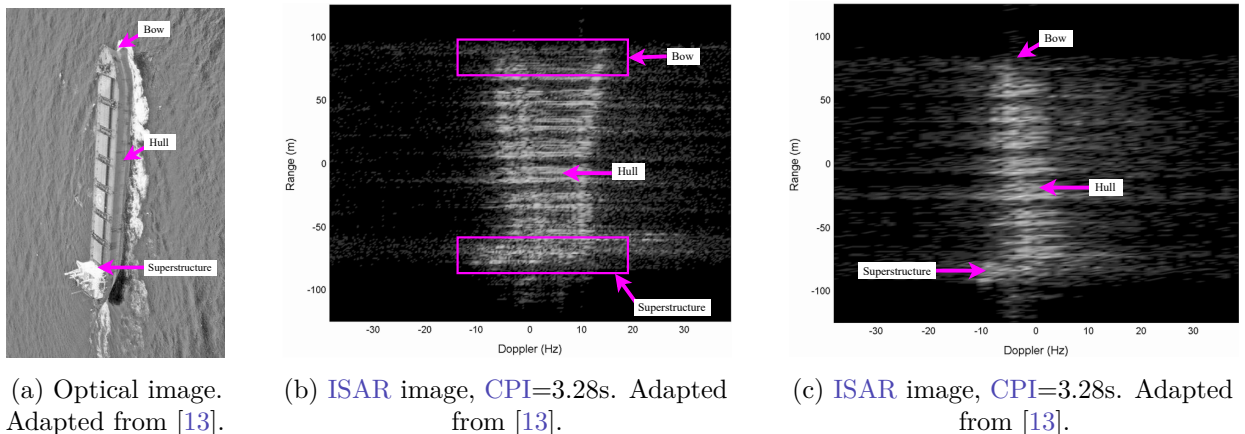


Figure 3.2: Optical and ISAR images of a bulk carrier ship to show how CPI affects focus of image.

The length of the **CPI** can be leveraged to generate more focused **ISAR** images. Case study 12.1 in [2] demonstrated that in cases where an object's motion varies over time, using smaller **CPIs** resulted in better-focused images. Various techniques for determining the optimal **CPI** have been developed. One such algorithm is presented in [13], which is an **IC**-maximization-based time windowing algorithm. This technique employs an iterative sliding window approach to identify the **CPI** that produces the highest **IC** value. It has been shown to be effective in improving the focus of **ISAR** images of large sea vessels. This improvement is illustrated in Figure 3.2(b) and (c) where the image becomes sharper with a shorter **CPI**.

However, the impact on imaging of small sea vessels was not investigated. Additional techniques for time windowing in both cooperative and non-cooperative sea vessel contexts are discussed in [3].

3.2.2 Focus vs Quality

Crucially, as highlighted by [6], a focused image does not necessarily equate to a high-quality image of the object. While **TMC** may enhance the image's focus, it cannot guarantee that the recorded data is of sufficient quality to produce a clear characterization of the object. As mentioned in [5], the quality of recorded data can be influenced by factors such as equipment setup, noise, clutter, and environmental conditions.

Furthermore, **ISAR** images are only suitable for feature extraction in classification when they possess high range and Doppler resolution, as stated in [6]. **TMC** serves to improve the range and Doppler resolution by enhancing image focus. Nevertheless, situations may arise where the image is well-focused, but the nature of the data restricts achieving high Doppler or range resolution. Although there is no existing literature addressing this specific issue in the field of **ISAR**, it is discussed in the context of other fields in [5] and [7], where poor-quality recorded data proves unsuitable for producing the anticipated results.

3.3 Translation Motion Compensation

As discussed in subsection 2.4.1, **TMC** algorithms are used to achieve focused **ISAR** imaged by compensating the effects of an object's undesired translation motion. The literature revealed many algorithms for both **RA** and **AF** as discussed throughout this section.

3.3.1 Range Alignment Algorithms

In [11] an investigation was conducted on how different **RA** techniques performed on range aligning maritime data of a *Umoya Omusha sailing yacht*. The investigation found the following results for different **RA** techniques.

- **Peak Alignment** is a simple **RA** algorithm that only uses cross-correlation to align the **HRRPs**. It assumes that the peak of each profile is a single **DS** and aligns adjacent profiles using their peaks. [11] revealed that this assumption led to misalignment of **HRRPs** when multiple **DSs** with varying intensity over the **CPI** existed. Additionally, the algorithm could only perform integer range bin shifting which also prevented perfect alignment of the **HRRPs**. However, despite these

limitations, it was shown to perform well on some of the measured data frames. An advantage of this algorithm is its low computation nature.

- **Envelope Correlation** is a widely used algorithm which has several variations, some of which were discussed in [11]. In its simplest form, the algorithm finds the number of shifts that maximises the cross-correlation between a reference profile and all other profiles. Like Peak Alignment, it can only perform integer bin shifts which limits its ability to align the profiles. In [11] several variations of the algorithm were investigated and all proved more effective at range aligning the measured **HRRPs** than peak alignment. However, the lower computation versions were only marginally better than Peak Alignment.
- **Global Method** is a **RA** technique that does not use cross-correlation. Instead it uses an optimisation algorithm to maximise the value of the sum envelope calculated for varying bin shifts [16]. In [11] it performed well on the maritime measured data. However, it uses optimisation which makes it a high-computation algorithm.

In [11], [17]'s algorithm that achieves fractional bin shifts was investigated. It proved less effective at aligning the maritime data **HRRPs** than the previously discussed algorithms. Additionally, it is an optimisation-based algorithm which makes it computationally expensive in nature. However, low computation algorithms that also achieve fractional bin shifts exist.

An example of such an algorithm was presented in [18], where **Haywood's RA** algorithm was introduced. This algorithm linearises the cross-correlation returns and applies them to the **HRRPs** in the frequency domain. This realises fractional bin shifts. In [6], this algorithm proved effective in realising range-aligned **HRRPs** for **ISAR** imaging.

3.3.2 Autofocus Algorithms

Many **AF** algorithms exist in the literature [19, 20, 2, 8], a few are discussed in this section.

- **Prominent Point Processing (PPP)** is an **AF** technique that uses information from the **DSS** to correct phase errors [2]. In [21], the **PPP** algorithm was performed on **HRRPs** of a boat. It was shown to be ineffective in producing a focused **ISAR** image when the algorithm was unable to accurately correct rotation motion. To do this effectively, exhaustive parameter searching is required [2] which is computationally expensive.
- **Image Contrast-Based Autofocus** attempts to focus the image by maximising the **IC**. Unlike **PPP**, it attempts to focus the entire image rather than a few points in the image. The case study conducted in [2] showed that the algorithm performed well on maritime data. However, it is a parametric algorithm¹ which makes it unsuitable for use in the context of non-cooperative sea vessels.

There exists a group of **AF** algorithms known as **Dominant Scatterer Algorithm (DSA)**. These algorithms use different approaches to select one or more range bins (scatterers) as the focused bin(s) which are subsequently used to correct all other range bins [19].

¹This algorithm uses known information about the object to compensate its undesirable motion.

- **SDSAF** is a type of **DSA** that uses a single range bin to perform phase correction on all range bins. One such algorithm is presented in [18]. This algorithm assumes the existence of a single bright **DS** in the image that remains consistently bright across all range profiles. During its development, it was observed that the algorithm did not consistently select the **DS** correctly, and the reason for this remained unclear. Nonetheless, the algorithm has been shown to produce well-focused **ISAR** images in other literature [6].
- **MDSAF** uses multiple range bins to perform phase correction on all other range bins. The algorithm presented in [8] was specifically developed for use in **ISAR** imaging of small sea vessels. The authors noted that prior to the development of their algorithm, existing **AF** algorithms had primarily been designed for application on large ships and aircraft. Several of these previous algorithms were found to be inadequate for use on small sea vessels. Other algorithms suitable for small sea vessels were found to be computationally expensive. Consequently, the authors developed a new, low-computation algorithm that uses a weighted sum of the phases of multiple **DS** to perform phase correction. The literature further showed that this new algorithm outperformed its predecessors in focusing sea vessels.

3.4 Quick-look Processors in Radar

For radar research to progress, access to large amounts of high-quality data is essential [5, 7]. The quality of data recorded by radar systems is impacted by various factors, including interference, equipment setup, and waveform parameters. As a result, in the absence of quality control systems, large recorded datasets only contain limited subsets that are suitable for use [5, 7]. In the context of **ISAR**, poor-quality data leads to images that, even when focused, remain unsuitable for feature extraction [6].

In [5], a **QLP** was developed to evaluate the quality of data recorded for the detection of small sea vessels. This **QLP** was specifically designed for the assessment of radar recordings during fieldwork. As such, a low-computation detection algorithm was employed. The processor was implemented in MATLAB and proved to be an effective solution for assessing the quality of field-recorded data.

Furthermore, in [7], a **QLP** designed to assess the quality of data collected for pulse compression and Doppler processing was developed. The **QLP** was specifically designed to operate on a low-resource system. Its primary purpose was to ensure that only high-quality radar recordings were retained after experiments. This processor was implemented in C++ and was proven to be an effective solution for its intended application.

Another system, detailed in [9], was developed for the real-time generation of medium-resolution airborne **Synthetic Aperture Radar (SAR)** images. Unlike the previously discussed systems, the focus was not on data quality assessment. Rather this system was aimed at real-time processing. It successfully achieved this objective, which shows that medium-resolution **SAR** images can be produced real-time.

Finally, in [21] an efficient **TMC** processing chain for **ISAR** images was developed. This processing chain underwent testing using an **ISAR** image of a large boat, with data collected using a chirp waveform.

The paper presented a comparative analysis between the developed chain and existing approaches, highlighting its superior ability to focus the image and its efficiency. The processing time for a single data frame of size 600×700 was demonstrated to be 0.4197 s. It is worth noting that while the chain was not tested on multiple ISAR frames or datasets, it clearly demonstrated that focused ISAR images of sea vessels can be generated when employing relatively low-computation algorithms.

3.5 Critical Review

It has become clear from the survey that the progression of ISAR imaging for sea vessels is beneficial to both civilian and military maritime applications. It was found that several complications exist in the imaging of sea vessels: their complex motion, the quality of rerecorded data and availability of TMC algorithms suitable for use on boats.

There are many TMC algorithms in existence. However, few have been specifically shown to perform well on large and small sea vessels. In [11], a study was conducted on how multiple RA algorithms performed on the same yacht. Several algorithms with varying levels of computation complexity were revealed. Similarly, various AF algorithms were found throughout the literature. However, no literature was found that compared the performance of low computation RA and AF algorithms on the same maritime dataset. Still, two low computation RA and AF autofocus techniques were revealed: Peak Alignment, Haywood's RA, SDSAF and MDSAF.

In other radar fields, [7, 5] found that the collection of poor quality data affected the development of the respective research fields. QLPs for quality assessment and control of recorded data were employed and proved useful. No literature was found of the use of such a system in the context of ISAR imaging of sea vessels. However, the survey did reveal literature where efficient systems were designed for medium-resolution SAR [9] and ISAR imaging [21]. This revealed that a system similar to those found in other radar fields could be achieved for ISAR imaging.

Chapter 4

Algorithm Verification and Validation

The [TMC](#) algorithms implemented in this chapter were chosen because of their low computation nature which made them desirable for use in a [QLP](#). Despite their simplistic nature, they have been shown to produce focused [ISAR](#) images in their respective literature [11, 18, 8]. Simulated data was used to verify that the implementation of each algorithm in MATLAB was correct. Thereafter, measured data was used to validate the implemented algorithms for use in the [QLP](#) designed in [chapter 5](#). The [CPI](#) and frame overlap percentage were kept constant at 128 [HRRPs](#) and 50 %, respectively.

4.1 ISAR Simulator

Simulated data was valuable for verifying that the algorithms investigated and implemented in this report functioned as expected. Since the ideal outcome of simulated data was known, it was used to reveal errors and limitations in the algorithm implementations.

The simulator considered for use in this report was a MATLAB script developed by Mustaqeem Aziz [22]. It used a [SFW](#) signal and user-defined x-y coordinates for scatterers to produce [HRRPs](#). The [HRRPs](#) were generated based on the configured rotation motion (in degrees per second) and translation motion (in meters per second).

4.1.1 Simulator Changes

Aziz's simulator [22] was adapted to better align with the data requirements for verifying the algorithms implemented in this report. [AF](#) algorithms use [DSs](#) to correct phase errors in the [HRRPs](#). These scatterers are selected based on power, amongst other criteria, which necessitated configurable Scatterer Amplitudes in the simulator. This allowed for some scatterers to be configured with higher power levels than others, which proved valuable in the verification of [DS](#) selection within the [AF](#) algorithms. Moreover, the Scatterer Amplitudes were configured using a Gaussian-like distribution. A simple [Command-line Interface \(CLI\)](#) was implemented to aid user-friendliness. The final simulator is available on [GitHub](#).

4.1.2 Description of Simulator Setup

The simulator was set-up as described in this subsection. The [SFW](#) parameters are described in [Table 4.1](#).

Parameter	Value
Center Frequency (f_0)	9.5 GHz
Frequency step (Δf)	4 MHz
Number of pulses (N)	256
Pulse Repetition Frequency (PRF)	2kHz
Number of Bursts (M)	32

Table 4.1: SFW parameters for simulation.

Additionally, the scatterers were setup as illustrated in Figure 4.1a. The simulated object was a representation of the boat in Figure 4.1b and included the boat's main features: 2 masts and a hull.

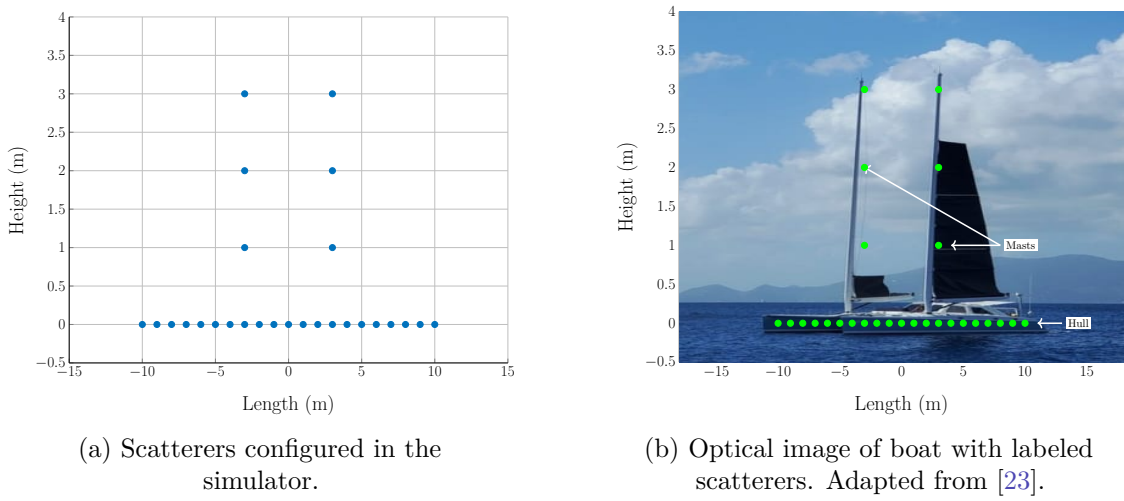


Figure 4.1: Scatterer structure used for simulation based on boat features.

Two sets of simulated data were used in this report. First, the object was simulated with a translation motion of **0 m/s** and rotation motion of **6 deg/s** to generate the ideal HRRPs and ISAR image shown in Figure 4.2. These served as a reference for what the profiles and ISAR image should look like after RA and AF. The boat features in Figure 4.1b are labelled in Figure 4.2b to show how the scatterers reflect in the ISAR image.

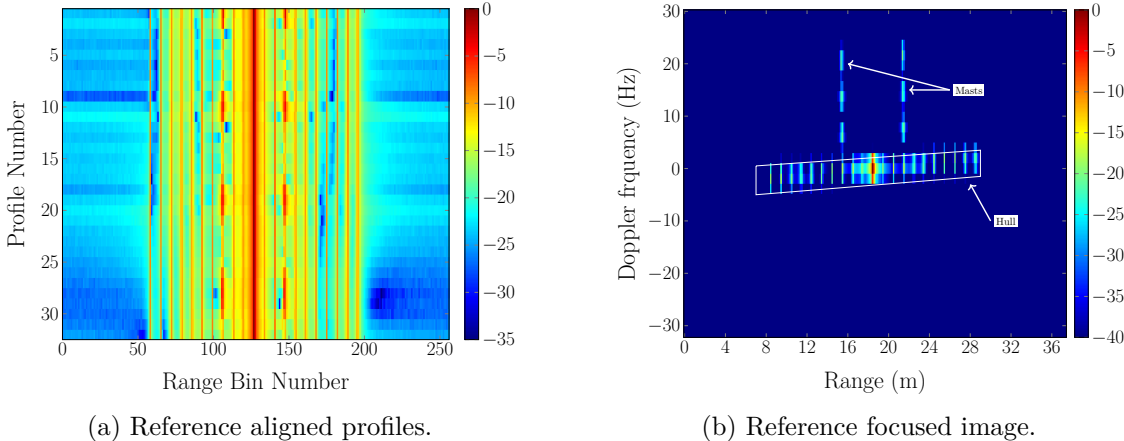


Figure 4.2: Simulated HRRPs and ISAR image for the object with 0 m/s translation motion and 6 deg/s rotation motion.

4.2. Description of Measured Data Setup

Additionally, the object was simulated to have a translation motion of **1 m/s** and rotation motion of **6 deg/s**, which produced the unaligned HRRPs and defocused ISAR image in Figure 4.3. In Figure 4.3b, the scatterers were spread over the Doppler and range axes which was not seen in Figure 4.2b. The scatterer smearing in Figure 4.3b was caused by the object's translation motion.

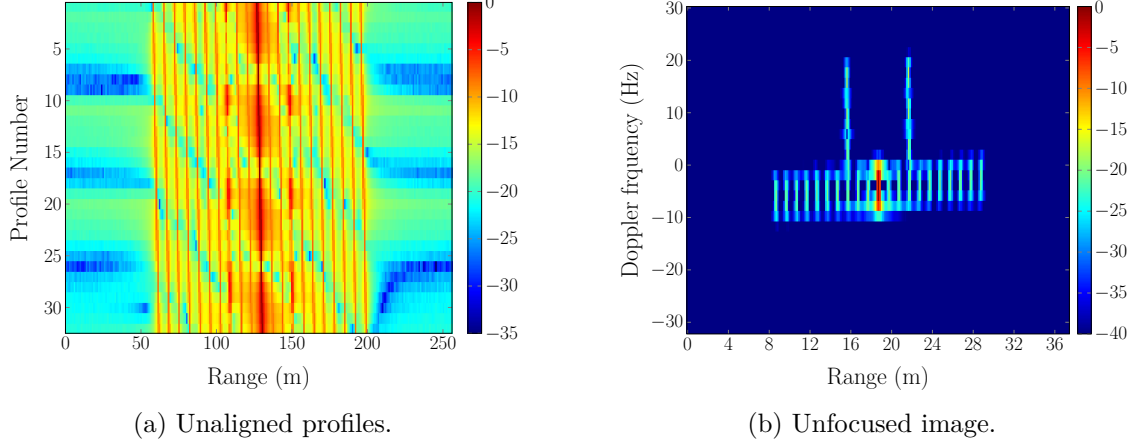


Figure 4.3: Simulated HRRPs and ISAR image for the object with 1 m/s translation motion and 6 deg/s rotation motion.

The testing code and configuration was collated into a single folder to facilitate repetition of the results achieved throughout this chapter. Furthermore, the RA and AF algorithms were added to the simulator script to simplify the testing process.

4.2 Description of Measured Data Setup

Measured HRRPs were used to validate the algorithms implemented in this report. The profiles were generated using a SFW fired at a *Zay-Yaan KB6* fishing boat moving toward the radar, further described in [1]. Figure 4.4 shows the boat that was used.

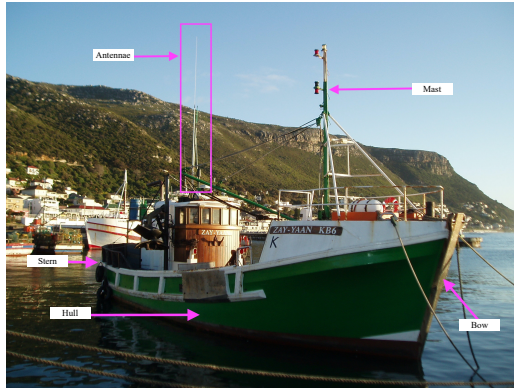


Figure 4.4: Optical image of Zay-Yaan KB6 fishing boat. Adapted from [1].

Several frames¹ were considered for use in validation. The ISAR image frames and HRRPs in Figure 4.5 were constructed from a single measured data set. As discussed in subsection 2.7.2, the size of the CPI affects the quality of the image. In this report, the CPI was fixed at 128 HRRPs, and it served as the

¹A frame is a single ISAR image developed using a pre-selected number of HRRPs. In this report it was 128 profiles.

4.2. Description of Measured Data Setup

constant value for all the frames. The frames considered in this section were chosen from the larger subset as they all produce ISAR images that resemble the side-view of the boat.

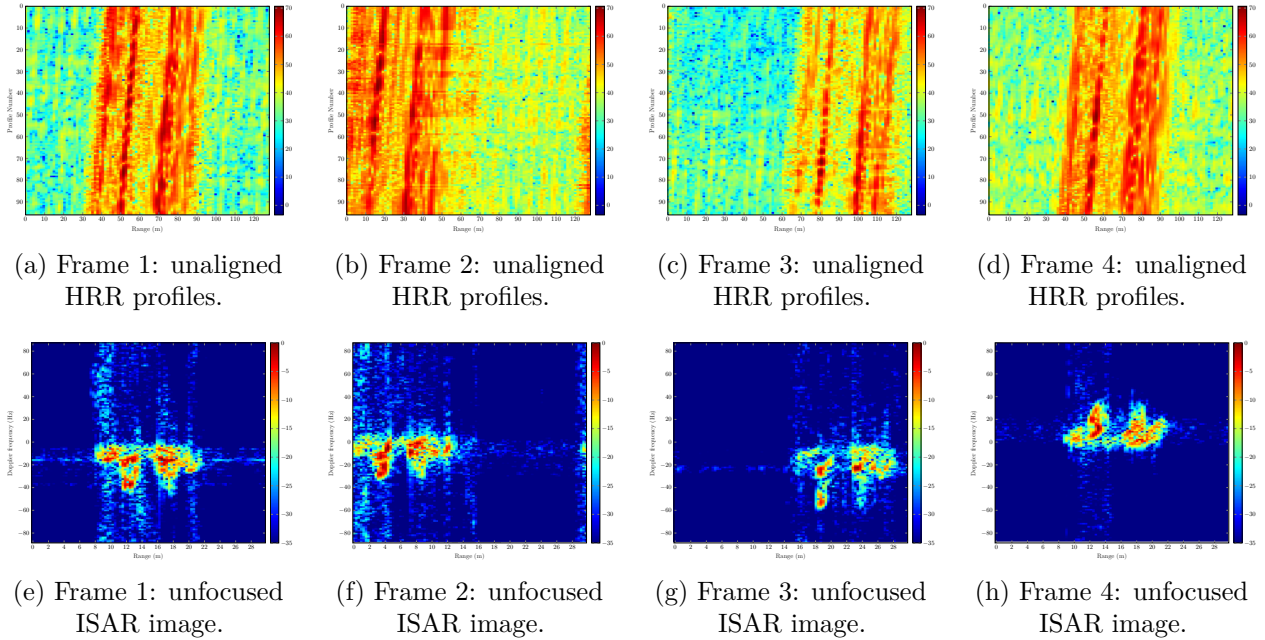


Figure 4.5: Different ISAR image frames produced from a single measured data set, before TMC was applied.

Multiple frames were unsuitable for validating the RA and AF algorithms discussed in this report due to specific characteristics. Figure 4.5b was not suitable because not all of the profiles appeared within the frame, which could have led to erroneous RA. Using this frame would have created uncertainty regarding whether any unexpected results were due to poor-quality data or the implemented algorithm, making it an unsuitable choice. Additionally, Figure 4.5c was significantly affected by noise and had fewer prominent scatterers compared to frames 1 and 2. This made it an unsuitable choice compared to the other frames.

Furthermore, the profiles in Figure 4.5a and 4.5d exhibited more than one clear DS and were completely within the frame, making them suitable choices for verifying RA algorithms. Figure 4.6 shows the HRRPs of these two frames after applying the Correlation RA algorithm.

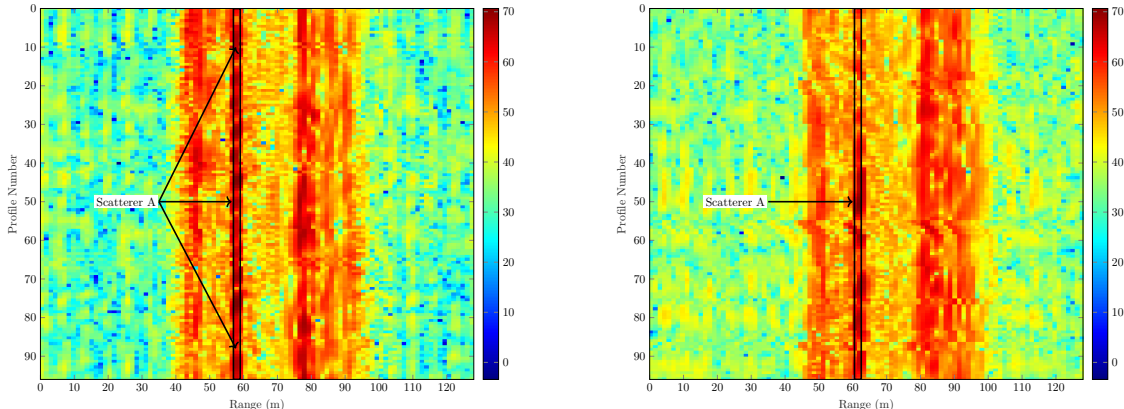


Figure 4.6: Range-aligned measured HRRPs: frame 1 (left) and 4 (right).

As discussed in chapter 2, not all frames of ISAR data can be focused due to factors such as the object's motion and the CPI. Consequently, it was expected that some measured data frames would not be perfectly range-aligned or autofocus. For the purpose of validation testing, it was essential to select ideal data that gave the TMC algorithms the best chance at success, since the aim was to demonstrate the performance of the algorithms on measured data.

When comparing the profile frames in Figure 4.6, it was clear that the profiles in frame 1 were better aligned than those in frame 4. Moreover, frame 1 featured a prominent Scatterer A that was consistently visible at range bin 57 across all range profiles, making it an ideal choice for AF validation. In contrast, Scatterer A in frame 4 did not exhibit the same level of consistent visibility in all profiles. Using frame 4 for validation testing would have introduced uncertainty surrounding whether any unexpected results in AF were caused by poor-quality data or the implemented algorithm. For these reasons, **frame 1 in Figure 4.6 was selected** for validation testing in this chapter.

A MATLAB script was used to facilitate the validation testing process. Permission was obtained from the CSIR to use their measured data but is not freely available for replicating the measured data results in this report.

4.3 Correlation Range Alignment Algorithm

This is a simplistic RA algorithm that uses cross-correlation to determine the number of integer range bins by which a profile is misaligned with respect to a reference profile. The calculated number of bins is used to shift the misaligned range profile into alignment with the reference profile. An outline of the correlation RA, as described in [11], is given in algorithm 1.

4.3.1 Pseudo Code and Implementation

```

input      : All HRRPs, matrix  $hrrp_{all}$ 
output     : Range-aligned HRRPs, matrix  $hrrp_{RA}$ 
parameter : Reference HRRP number,  $refIndex$ 

1 begin
2    $hrrp_{ref} \leftarrow hrrp_{all}[refIndex]$ 
3    $correlation \leftarrow$  auto-cross-correlate  $hrrp_{ref}$ 
4    $peakIndex_{ref} \leftarrow$  index of  $\max(correlation)$ 
5   for  $k$  in 1 to  $\text{rows}(hrrp_{all})$  do
6      $correlation \leftarrow$  cross-correlate  $hrrp_{all}[k]$  and  $hrrp_{ref}$ 
7      $peakIndex \leftarrow$  index of  $\max(correlation)$ 
8      $shift \leftarrow peakIndex_{ref} - peakIndex$ 
9      $hrrp_{RA}[k] \leftarrow circularshift hrrp_{all}[k]$  by  $shift$ 
10  end
11 end
```

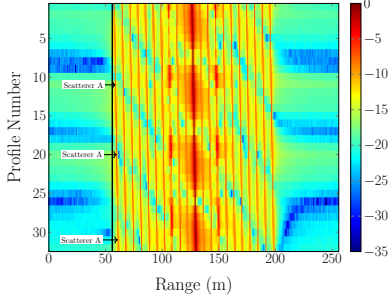
Algorithm 1: Correlation RA Algorithm.

4.3. Correlation Range Alignment Algorithm

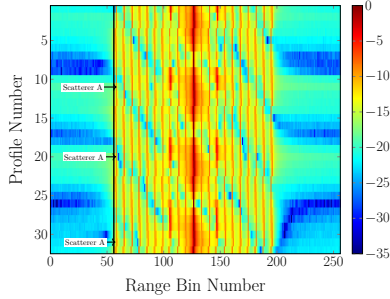
The Correlation Algorithm, [algorithm 1](#), was implemented as a stand-alone function in MATLAB. The function, `corrRA.m`, was validated and verified in this section.

4.3.2 Algorithm Verification

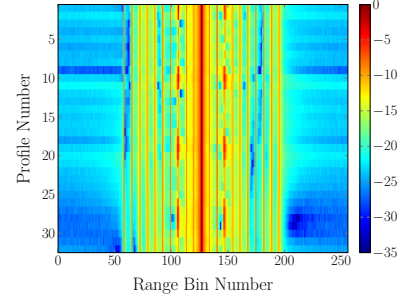
In this subsection simulated HRRPs were used to verify that [algorithm 1](#) was implemented correctly in MATLAB.



(a) Unaligned profiles.



(b) Range-aligned profiles.



(a) Reference aligned profiles.

Figure 4.7: Simulated HRRPs before and after Correlation RA.

Figure 4.8: Simulated object with 0 m/s translation motion.

Recall from [subsection 2.5.1](#) that an object's motion causes it to change position between range profiles. [Figure 4.7a](#) shows that Scatterer A migrated between profiles as expected, the vertical line further illustrates that the profiles were not aligned. Correlation RA was applied to the unaligned profiles in an attempt to achieve straight line scatterers similar to profiles of the object with 0 m/s translation motion shown in [Figure 4.8a](#).

Using line 7 of [algorithm 1](#), the peak location (index) of each profile's cross-correlation with respect to profile 1 was calculated. This value was then used to calculate the number of bins each profile was shifted from profile 1 as in line 8 of [Figure 4.7a](#). [Figure 4.9](#) shows the calculated bin shifts for each profile in [Figure 4.9](#).

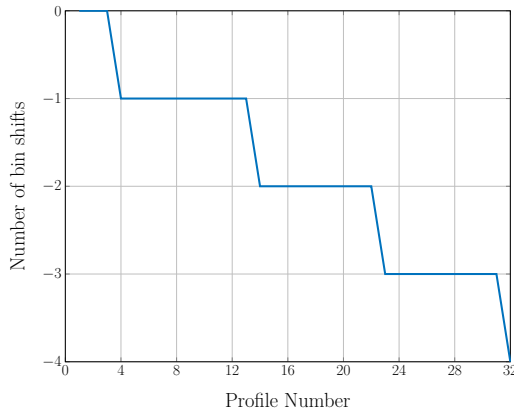


Figure 4.9: Staircase curve of range bin shifts per simulated HRRP for Correlation RA.

[Figure 4.7a](#) shows that Scatterer A migrated by a fraction of a range bin between successive profiles.

However, the 'steps' in Figure 4.9 show that each profile was always shifted by an integer number of bins. As explained before, the bin shifts were calculated as the difference between array indices which was an integer value. Therefore, profiles with fractional bin shifts were rather treated as a full bin shift as shown by the flat horizontal steps in Figure 4.9. Similar results were seen in the literature [11].

Overall, when the implemented [algorithm 1](#) was applied on the unaligned profiles in Figure 4.7a, range-aligned profiles were not produced in Figure 4.7b. However, the range-aligned profiles did follow the staircase pattern of Figure 4.9. Although, the profiles were not perfectly aligned as expected, they were correctly aligned in terms of the bin shift values in Figure 4.9. These results were in agreement with the results in [11], therefore [algorithm 1](#) was implemented correctly.

4.3.3 Algorithm Validation

In this subsection, measured [HRR](#) data was used to validate the Correlation [RA](#) implementation for use in the [QLP](#) designed in this report.

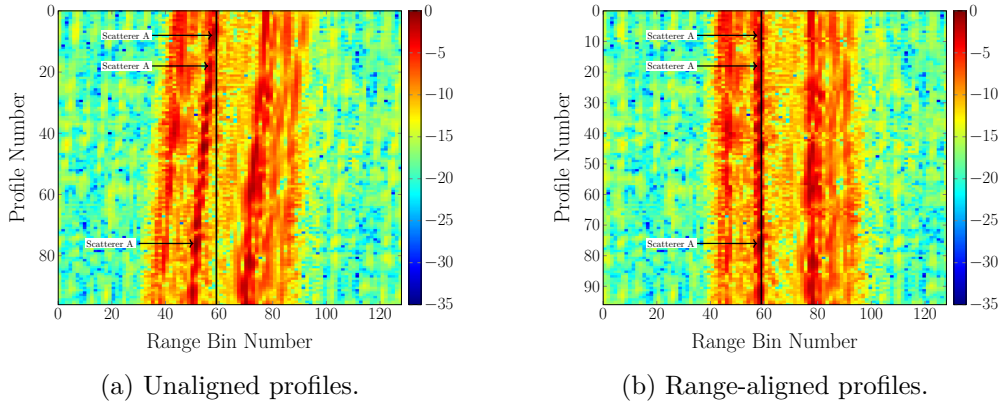


Figure 4.10: [HRRPs](#) of a measured data frame before and after Correlation [RA](#).

Figure 4.10a shows that Scatterer A migrated between profiles. Comparing the position of Scatterer A, in all profiles, to the vertical black line in Figure 4.10a illustrates that before [RA](#), the profiles were not aligned to profile 1.

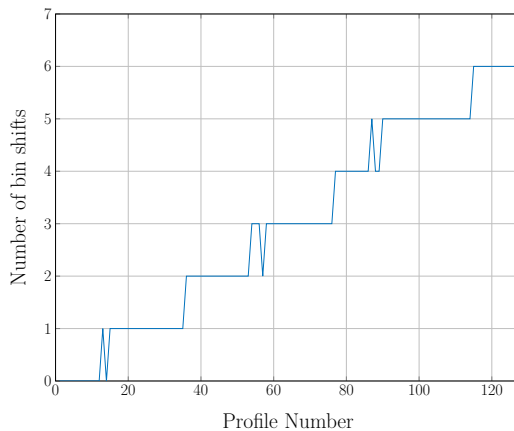


Figure 4.11: Staircase curve of range bin shifts per measured [HRRP](#) for Correlation [RA](#).

Figure 4.11 shows the bin shifts for all profiles, calculated with respect to profile 1 in Figure 4.10a. These shifts were applied to the unaligned profiles and resulted in the range-aligned profiles in Figure 4.10b.

Figure 4.10b shows that after range-alignment, Scatterer A remained in the same range bin throughout all profiles. Additionally, all scatterers were aligned with the vertical black line. Therefore, performing Correlation RA range-aligned the profiles and was validated for use in this report.

4.4 Haywood's Range Alignment Algorithm

This RA algorithm realised fractional bin shifts, unlike the integer-only range bin shifts allowed in algorithm 1. This is achieved by linearising the calculated bin shifts and applying them to the profiles as a phase shift, ϕ . An outline of the Haywood RA algorithm, as described by [18, 6], is given in algorithm 2.

4.4.1 Pseudo Code and Implementation

```

input      : All HRRPs, matrix  $hrrp_{all}$ 
output    : Range-aligned HRRPs, matrix  $hrrp_{RA}$ 
parameter: Reference HRRP number,  $refIndex$ 

1 begin
2    $hrrp_{ref} \leftarrow hrrp_{all}[refIndex]$ 
3   for  $k$  in 1 to  $rows(hrrp_{all})$  do
4      $correlation[k] \leftarrow$  cross-correlate  $hrrp_{all}[k]$  and  $hrrp_{ref}$ 
5      $peakIndex[k] \leftarrow$  index of  $\max(correlation[k])$ 
6   end
7    $shifts \leftarrow$  linearise  $peakIndex$ 
8    $N \leftarrow \text{length}(shifts)$ 
9   for  $k$  in 1 to  $rows(hrrp_{all})$  do
10    for  $n$  in 1 to  $N$  do
11       $\phi[n] \leftarrow \exp(-j \cdot shifts[k] \cdot \frac{n}{N})$ 
12    end
13     $hrrp_{RA}[k] \leftarrow IFFT(\phi \cdot FFT(hrrp_{all}[k]))$ 
14  end
15 end
```

Algorithm 2: Haywood RA Algorithm.

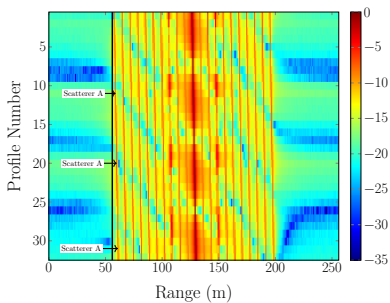
The RA algorithm, algorithm 2, was implemented as a stand-alone function in MATLAB. The implementation, `haywoodRA.m`, was validated and verified in this section.

4.4.2 Algorithm Verification

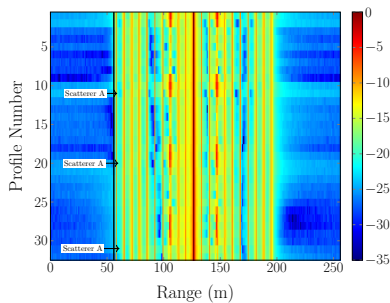
In this subsection simulated HRRPs were used to verify that algorithm 2 was implemented correctly in MATLAB.

4.4. Haywood's Range Alignment Algorithm

The vertical black line in Figure 4.12b shows that the range profiles were not originally aligned. Haywood's RA algorithm was applied to the unaligned profiles in an attempt to align them such that Scatterer A remained in the same range bin across all profiles. Figure 4.13a serves as a reference for what range-aligned profiles should look like.

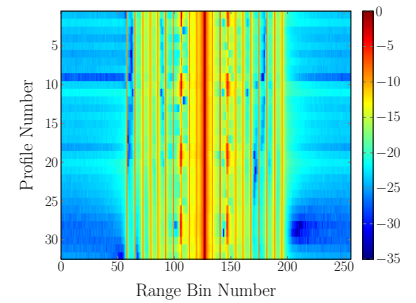


(a) Unaligned profiles.



(b) Range-aligned profiles.

Figure 4.12: Simulated HRRPs before and after Haywood RA.



(a) Reference aligned profiles.

Figure 4.13: Simulated object with 0 m/s translation motion.

The blue 'staircase' curve in Figure 4.14 shows the bin shifts calculated using lines 3 to 6 of algorithm 2 and the red line shows the linearised shifts as per line 7 of algorithm 2. The red line further shows that fractional bin shifts were calculated in the implementation as expected.

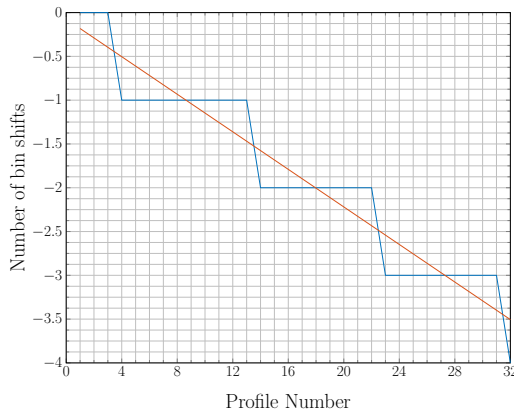


Figure 4.14: Linearised staircase curve of range bin shifts per simulated HRRP for Haywood RA.

In Figure 4.12b Scatterer A remained in the same range bin in all the profiles and shows that the calculated bin shifts successfully range-aligned the profiles. Comparing the scatterer lines to the vertical black line further proves that the profiles are aligned after Haywood RA. Therefore, Haywood RA yielded the expected result which verified that algorithm 2 was implemented correctly.

4.4.3 Algorithm Validation

In this subsection, measured HRRPs were used to validate the Haywood RA implementation.

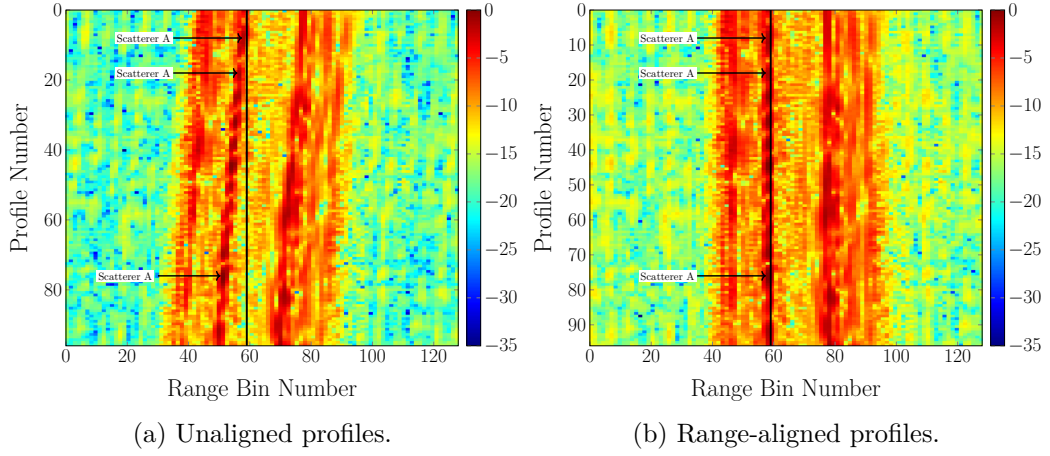


Figure 4.15: HRRPs of a measured data frame before and after Haywood RA.

Figure 4.15a shows that Scatterer A migrated between profiles and that before RA, the profiles were not aligned to profile 1. Figure 4.16 shows the calculated bin shifts for the unaligned profiles which were calculated with respect to profile 1. Figure 4.15b shows that, after range-alignment, Scatterer A did not migrate between profiles and that all scatterers were aligned with the vertical black line. Therefore, Haywood RA range-aligned the profiles and was validated for use in this report.

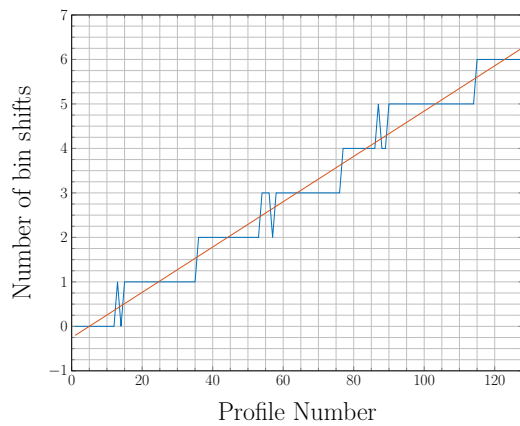


Figure 4.16: Linearised staircase curve of range bin shifts per measured HRRP for Haywood RA.

4.5 SDSAF Algorithm

This is a type of DSA that uses a single scatterer to correct the phase errors that remain after RA. A set of selection criteria is used to choose the DS and its phase is used to correct all other HRRPs. The SDSAF algorithm, as described by [18], was outlined in [algorithm 3](#).

4.5.1 Pseudo Code and Implementation

```

input      : Range-aligned HRRPs, matrix  $hrrp_{RA}$ 
output    : Autofocused HRRPs, matrix  $hrrp_{AF}$ 

1 begin
2    $scattererPower \leftarrow 0$ 
3   for  $k$  in 1 to  $\text{rows}(hrrp_{RA})$  do
4     for  $n$  in 1 to  $\text{columns}(hrrp_{RA})$  do
5        $scattererPower \leftarrow scattererPower + |hrrp_{RA}[k][n]|^2$ 
6     end
7      $allPower[k] \leftarrow scattererPower$ 
8   end
9    $avgPower \leftarrow mean(allPower)$ 
10   $candidateIndices \leftarrow \text{indices of } allPower > avgPower$ 
11  for  $b$  in 1 to  $\text{length}(candidateIndices)$  do
12    for  $k$  in 1 to  $\text{rows}(hrrp_{RA})$  do
13       $amplitudes[k] \leftarrow |hrrp_{RA}[k][candidateIndices[b]]|$ 
14    end
15     $variance[i] \leftarrow variance(amplitudes)$ 
16  end
17   $DSIndex \leftarrow candidateIndices[\text{index of } \min(variance)]$ 
18  for  $k$  in 1 to  $\text{rows}(hrrp_{RA})$  do
19     $angle \leftarrow angle(hrrp_{RA}[k][DSIndex])$ 
20     $phaseHistory[k] \leftarrow exp(-1i \cdot angle)$ 
21  end
22  for  $k$  in 1 to  $\text{rows}(hrrp_{RA})$  do
23    for  $n$  in 1 to  $\text{columns}(hrrp_{RA})$  do
24       $hrrp_{AF}[k][n] \leftarrow hrrp_{RA}[k][n] \cdot phaseHistory[k]$ 
25    end
26  end
27 end

```

Algorithm 3: Single Dominant Scatterer AF Algorithm.

The SDSAF algorithm, [algorithm 3](#), was implemented as a stand-alone MATLAB function. The implemented function, [haywoodAF.m](#), was validated and verified in this section.

4.5.2 Algorithm Verification

As discussed in [subsection 2.5.2](#), after RA, AF is used to correct phase errors that cause Doppler spreading in the ISAR image. Correlation range-aligned simulated HRRPs were used to verify that [algorithm 3](#) was implemented correctly in MATLAB.

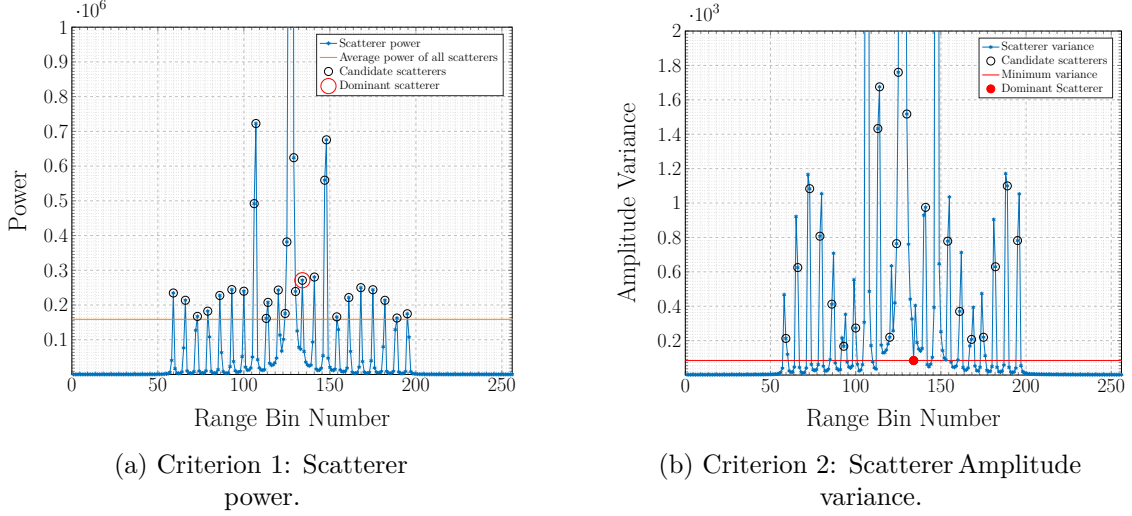


Figure 4.17: SDSAF DS selection for Correlation range-aligned simulated HRRPs.

In [algorithm 3](#), lines 10 and 17 outline the criteria for selecting the DS, which is used to phase-correct HRRPs. Line 10 outlines the conditions for candidate DS selection. [Figure 4.17a](#) shows that all the chosen candidate scatterers were above the average power threshold (indicated by the orange line). [Figure 4.17b](#) illustrates the implemented DS selection process based on the criterion defined in line 17 of [algorithm 3](#). [Figure 4.17b](#) shows that the selected DS had the least amplitude variance (indicated by the red line), which aligns with the conditions of criterion 2. Therefore, both selection criteria were implemented correctly.

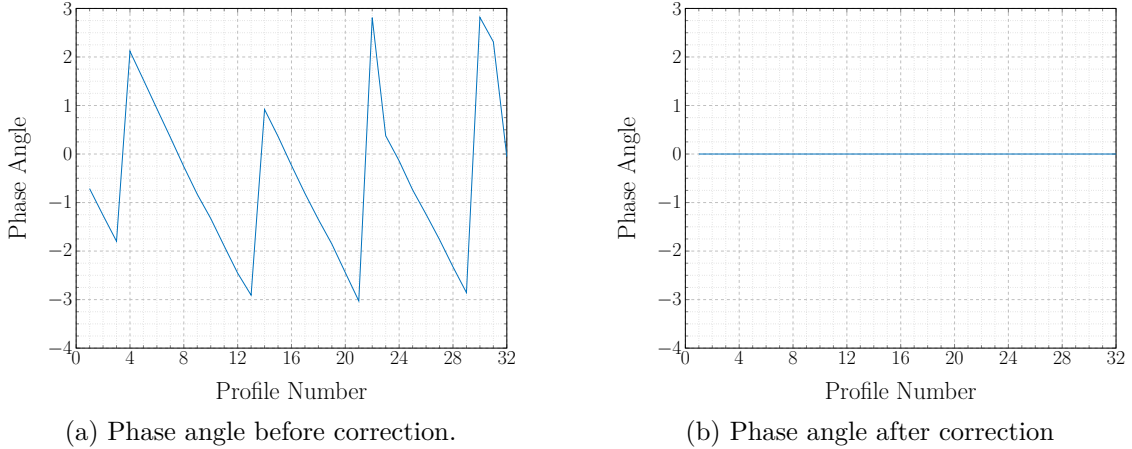


Figure 4.18: DS phase angle before and after SDSAF phase correction on simulated data.

As outlined in lines 18-21 of [algorithm 3](#), the phase history of the DS was computed as the conjugate of the angle through which the DS moved between profiles. This value was then used to perform phase correction on all profiles. The plot in [Figure 4.18b](#) illustrates that, following phase correction, the angle of the DS was effectively zero, as expected. Additionally, the white horizontal line in [Figure 4.19](#) shows that the DS was centered on zero-Doppler after AF. These results collectively confirm that phase correction was implemented correctly.

[Figure 4.20c](#) shows the image of the object with no translation motion, and represents the ideal focused image after RA and AF. The scatterer coordinates in [Figure 4.1a](#) show that the simulated ship had a

single, thin hull and two masts. Figure 4.20c shows the hull and mast features clearly.

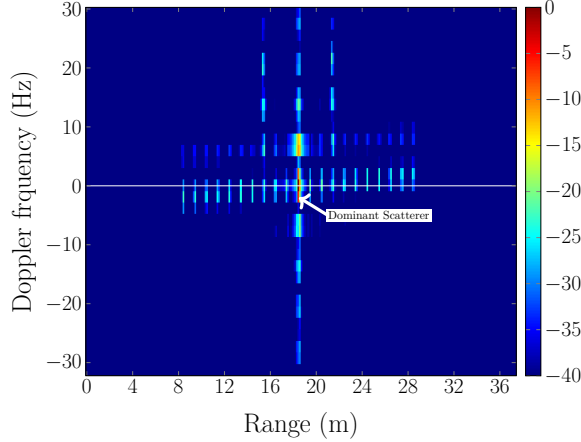


Figure 4.19: ISAR image formed after SDSAF correction on Correlation range-aligned simulated HRRPs.

However, in Figure 4.20a, a duplication of the hull, seen as two similar sets of bright scatterers labelled A and B, appeared due to Doppler spreading caused by phase errors in the HRRPs. To address this, SDSAF was applied to the Correlation range-aligned profiles. Consequently, Figure 4.20a shows a more focused image, featuring a single prominent group of scatterers representing the hull. IC values were used to quantitatively evaluate the SDSAF's performance. The IC values were **24.73** for the image before AF and **34.09** for the image after AF. The improvement of the IC after SDSAF further confirmed that SDSAF improved the focus of the image. Therefore, algorithm 3 was implemented correctly.

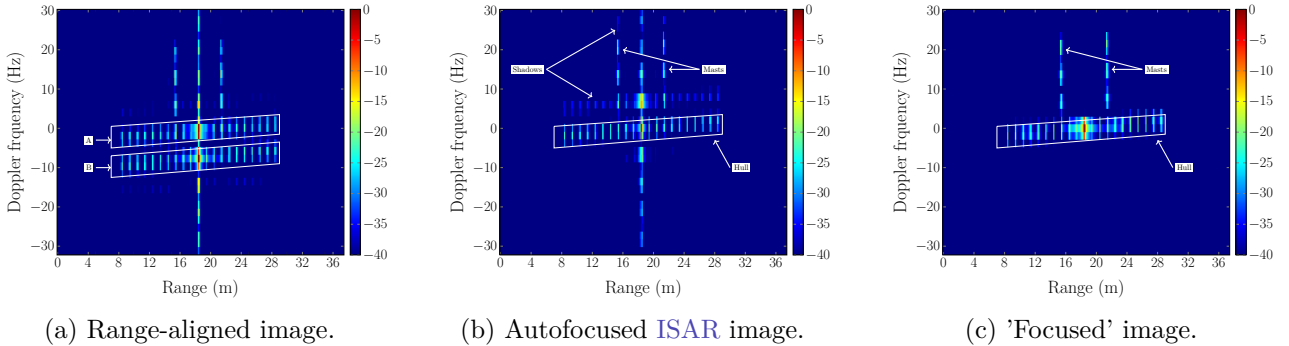


Figure 4.20: (a) Correlation range-aligned simulated ISAR image, (b) SDSAF autofocus simulated ISAR image, (c) ISAR image of simulated object with 0 m/s translation motion.

Importantly, while the implementation was correct, comparing Figure 4.20b to Figure 4.20c shows that the image remained defocused after AF. In Figure 4.20b the DS, at 18.5m, is spread over the Doppler axis which also appears in Figure 4.20a. This spreading was a result of poor RA by the Correlation RA algorithm, as discussed in subsection 4.4.2. Additionally, in Figure 4.20b the ship's hull and masts appear to have faint scatterer sidelobes. This shows that the SDSAF algorithm did not perfectly correct the scatterer phases. This is also attributed to using misaligned range profiles. Nevertheless, the image was still more focused after RA and the SDSAF was implemented correctly.

4.5.3 Algorithm Validation

In this subsection, measured Correlation range-aligned HRR data was used to validate that algorithm 3 improved the focus of the ISAR image. Figure 4.21a shows the original image formed using uncompensated HRRPs. Figure 4.21b shows the image formed using the Correlation range-aligned profiles and was included for discussions around the performance of AF.

Before comparing the ISAR images, it is important to recall that sidelobes formed when using the FFT on measured data can result in Doppler spreading in the images, as discussed in section 2.7 of chapter 2. Windowing was applied to minimise these sidelobes, but was not completely effective, as is evident in the images throughout this section. The spectral spreading caused by these sidelobes was present in the range-aligned image, and persisted in the autofocused images. Whilst the phase correction performed in AF can reduce the sidelobes in measured data, it is not the purpose of the algorithm.

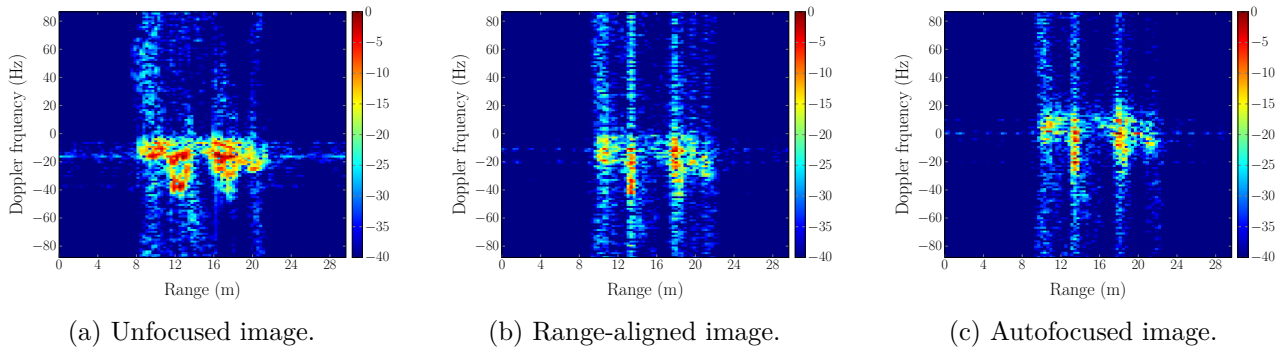


Figure 4.21: ISAR images formed using the original, Correlation range-aligned and SDSAF autofocus HRRPs of a single measured data frame.

In Figure 4.21a, the features of the object were significantly spread over both the range and Doppler axes. This resulted in an poor representation of the boat's features shown in Figure 4.22, for instance, the mast and antennae were wider in range than expected. Figure 4.21b shows that after RA, the spreading in the range axis was reduced as can be seen by the thinner mast and antennae. However, there was still significant spreading of the object's features over the Doppler axis, which was attributed to the effects of phase errors in the range-aligned profiles and sidelobes in the data.

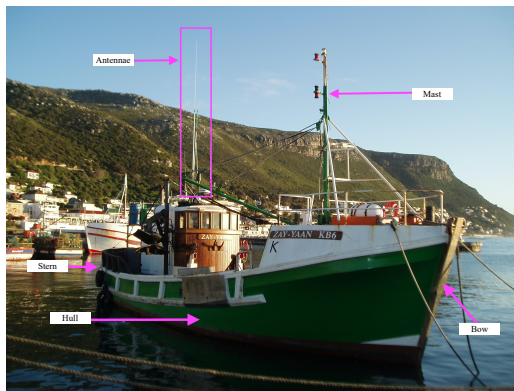


Figure 4.22: Optical image of Zay-Yaan KB6 fishing boat. Adapted from [1].

As discussed in subsection 2.5.2, AF is used to correct the phase errors introduced by RA. Figure 4.21c

shows that after **AF** was applied, the Doppler spreading was reduced; however, the shape of the bow and mast were not an accurate representation of the features in Figure 4.22. The **IC** values of each image were **7.0534**, **8.1803**, and **10.4345** for the unfocused, range-aligned, and autofocus images, respectively. Although there was a $\frac{10.4345 - 7.0534}{7.0534} = 47.94\%$ improvement on the image contrast after **RA** and **AF** was applied, the image in Figure 4.21c was still defocused.

Importantly, in measured data there often exists more than one **DS**. A limitation of the SDSAF algorithm is that it uses only one **DS** to phase correct all profiles. The poor quality of Figure 4.21c was attributed to the **DS** selected by the SDSAF algorithm. As discussed in the literature [18], the algorithm is known to, in some instances, select the incorrect Scatterer As the **DS**. The reasons behind this were unknown to the authors of [18].

As explained in subsection 2.7.1 of chapter 2, the **SNR** of a scatterer is influenced by noise, which subsequently impacts the performance of **AF** algorithms. Figure 4.23 shows that a low power **DS** was selected when producing Figure 4.21c.

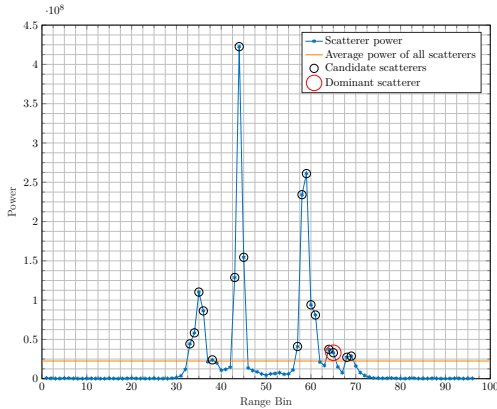


Figure 4.23: Scatterer power for the selection of a **DS** in SDSAF applied to correlation range-aligned measured HRRPs.

Consequently, whilst multiple **DS**s cannot be selected, a different approach was taken to improve the performance of the algorithm. A **SF** was introduced into line 10 of algorithm 3 to ensure that a higher power **DS** was selected. The aim was to improve the quality of the autofocus image by selecting a **DS** that was less affected by noise. This was implemented as shown in Listing 4.1.

```
1 scaling_factor = 10;
2 candidate_scatterers_idx = find(power_scatterer>scaling_factor*average_power_scatterer);
```

Listing 4.1: MATLAB code for scaling factor in candidate **DS** selection.

Two scaling factors, namely 5 and 10, were used to test the effect of the improved implementation on the performance of SDSAF. Figure 4.24a and Figure 4.24b show that as the **SF** increased, a higher power **DS** was selected as expected.

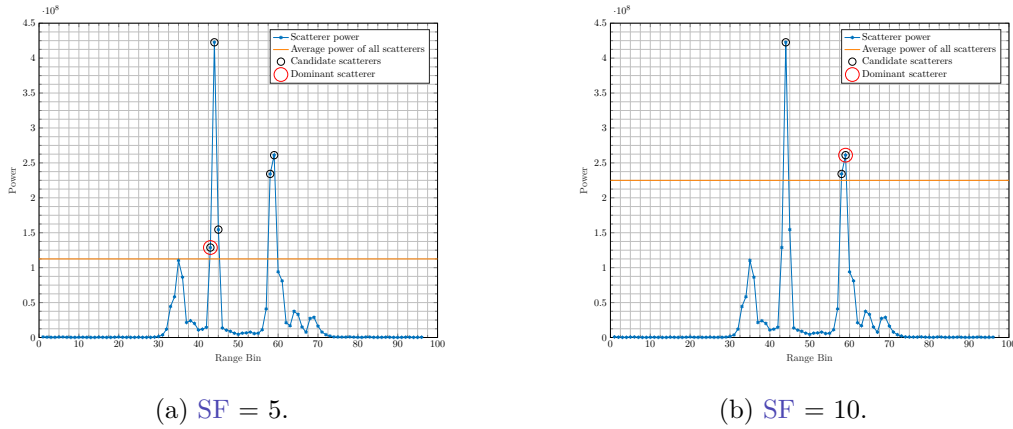


Figure 4.24: Scatterer power for the selection of a DS in SDSAF using various threshold SFs applied to Correlation range-aligned measured HRRPs.

Subsequently, introducing the **SF** produced the images in Figure 4.25. Figure 4.25a shows the focused image before the **SF** was introduced which inherently means that the **SF** was 1. The **IC** values for each image were calculated to provide a quantitative evaluation of the **SF**'s effect on the performance of **SDSAF**. The values for images (a),(b) and (c) in Figure 4.25 were calculated as **10.4345**, **15.1049** and **15.2911** respectively. The improvement of the **IC** values as the **SF** increased, indicated that introducing the **SF** improved the performance of **SDSAF**.

Although the IC values indicated that Figure 4.25b and Figure 4.25c were similarly focused, the visual results did not reflect his result. In Figure 4.25b, object was more spread over the Doppler axis than in Figure 4.25a. In contrast, when a SF of 10 was used, Figure 4.25b showed that the object was less spread over the Doppler axis than in Figure 4.25a. This resulted in a more accurate representation of the boat's features: there was a distinct long, thin rectangular cluster of scatterers representing the antennae and the angular bow and rounded stern were clearly identifiable.

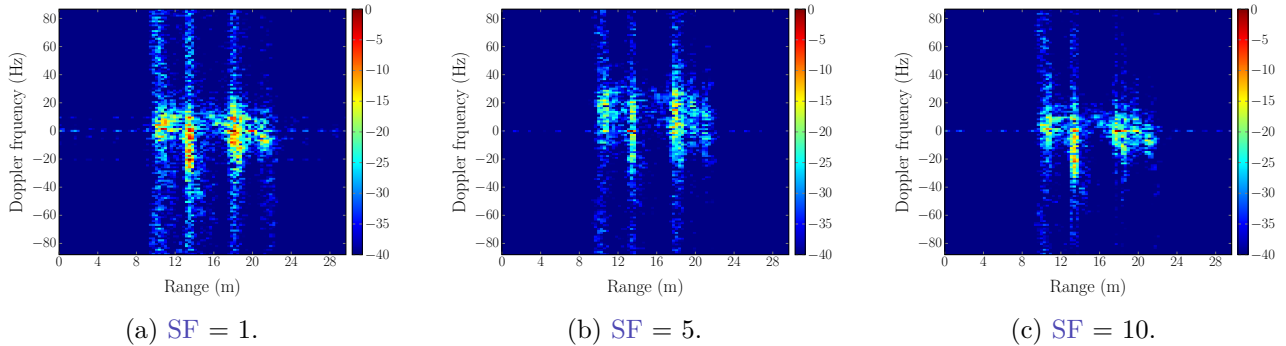


Figure 4.25: ISAR images after SDSAF using different SFs applied to Correlation range-aligned measured HRRPs.

Therefore, the **SF** improved the performance of **SDSAF**, resulting in a more focused image. Using a **SF** of 10 produced an image which more accurately represented the features on the boat than the image produced when no **SF** was used. However, when a scaling factor of 5 was used, the image appeared less focused. This was attributed to the selection of an unsuitable **DS**. Importantly, this does not imply that a **SF** of 5 is inherently less desirable than a **SF** of 1. Rather, it was a consequence of the characteristics of the data and could occur regardless of the chosen **SF**.

Overall, the improved SDSAF implementation produced a focused ISAR image when using a SF of 10 and was validated for use in this report. This SF of 10 was used for all following experimentation which involved SDSAF.

4.6 MDSAF Algorithm

The MDSAF algorithm is a type of DSA that uses a set of scatterers to phase correct HRRPs. The DSs are selected as those with the least dispersion². The MDSAF algorithm, as described in [8], was outlined in [algorithm 4](#).

²Dispersion describes the spread of the Scatterer Across all HRRPs

4.6.1 Pseudo Code and Implementation

```

input      : All HRRPs, matrix  $hrrp_{all}$ 
output     : Range-aligned HRRPs, matrix  $hrrp_{RA}$ 
parameter: Reference HRRP number,  $refIndex$ 

1 begin
2    $scattererAmplitudes \leftarrow 0$ 
3   for  $k$  in 1 to  $rows(hrrp_{RA})$  do
4     for  $n$  in 1 to  $columns(hrrp_{RA})$  do
5        $scattererAmplitudes \leftarrow scattererAmplitudes + |hrrp_{RA}[k][n]|^2$ 
6     end
7      $mean[n] \leftarrow mean(scattererAmplitudes)$ 
8      $variance[n] \leftarrow var(scattererAmplitudes)$ 
9   end
10   $a \leftarrow 0$ 
11  for  $b$  in 1 to  $length(mean)$  do
12     $dispersion[b] \leftarrow variance[b]/(variance[b] + mean[b]^2)$ 
13    if  $dispersion > 0.16$  then
14       $candidateIndices[a] \leftarrow b$ 
15       $a \leftarrow a + 1$ 
16    end
17  end
18   $candidateIndices_{sorted} \leftarrow$  indices of ascending sort
19   $dispersion(candidateIndices)$ 
20   $DSindices \leftarrow candidateIndices_{sorted}[1 \text{ to } 11]$ 
21  for  $b$  in 1 to  $length(DSindices)$  do
22    for  $k$  in 1 to  $rows(hrrp_{RA})$  do
23       $product[k][b] = conjugate(hrrp_{RA}[refIndex][b]) \cdot hrrp_{RA}[k][b]$ 
24    end
25  end
26  for  $k$  in 1 to  $rows(product)$  do
27     $angle \leftarrow angle(mean(product[k]))$ 
28     $phaseShift[k] \leftarrow exp(-1i \cdot angle)$ 
29  end
30  for  $k$  in 1 to  $rows(hrrp_{RA})$  do
31    for  $n$  in 1 to  $columns(hrrp_{RA})$  do
32       $hrrp_{AF}[k][n] \leftarrow hrrp_{RA}[k][n] \cdot phaseShift[k]$ 
33    end
34  end

```

Algorithm 4: Multiple Dominant Scatterer AF Algorithm.

The MDSAF algorithm was implemented as a stand-alone MATLAB function. The implemented function, `yuanAF.m`, was validated and verified in this section.

4.6.2 Algorithm Verification

Correlation range-aligned simulated HRRPs were used to verify that [algorithm 4](#) was implemented correctly in MATLAB.

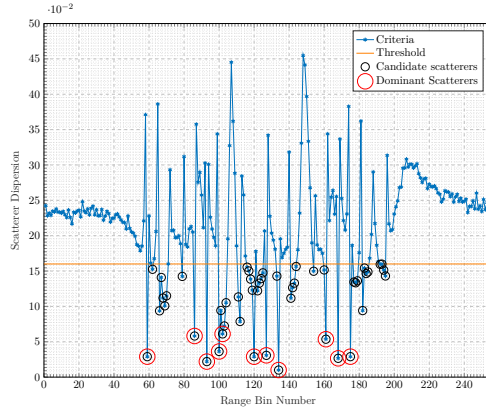


Figure 4.26: MDSAF DS selection for Correlation range-aligned simulated HRRPs.

[Figure 4.26](#) shows the candidate DSs selected based on the criterion outlined in lines 11-16 of [algorithm 4](#). All scatterers that had a dispersion value below the 0.16 threshold (indicated by the orange line) were selected as candidate scatterers, while those above the threshold line were not chosen. Therefore, the candidate scatterer selection was implemented correctly.

In [algorithm 4](#), lines 17 and 18 outline the process for selecting the DSs as the 11 scatterers with the smallest dispersion value. The larger red circles in [Figure 4.26](#) show that the smallest 11 dispersion-valued candidate scatterers were chosen as the DSs as expected. This verifies that the DS selection was implemented correctly.

In line 22 of [algorithm 4](#) a reference profile is used, [8] does not clarify how to choose this profile. Rather than selecting it as an arbitrary value, a step was introduced to select the reference profile as the profile in which the sum of powers from all the selected DSs was the greatest. The reasoning behind this was that the reference profile would be selected as the profile where the scatterers are the most concentrated and likely their original position so any spreading from that point would be due to motion and should be shifted back to that original position. The implementation of this selection is shown in [Listing 4.2](#).

```
1 [~, ref_HRRP_num] = max(sum(abs(RA_HRRP(:, DS_idx)).^2, 2));
```

Listing 4.2: MATLAB code for selecting reference profile.

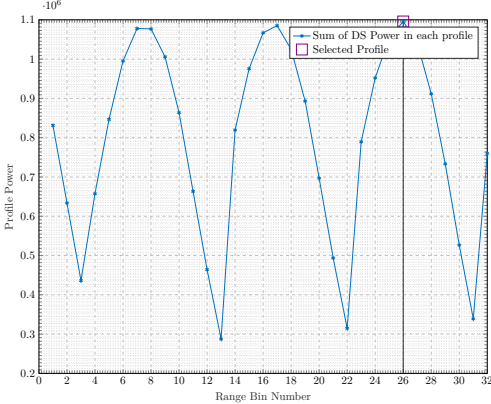
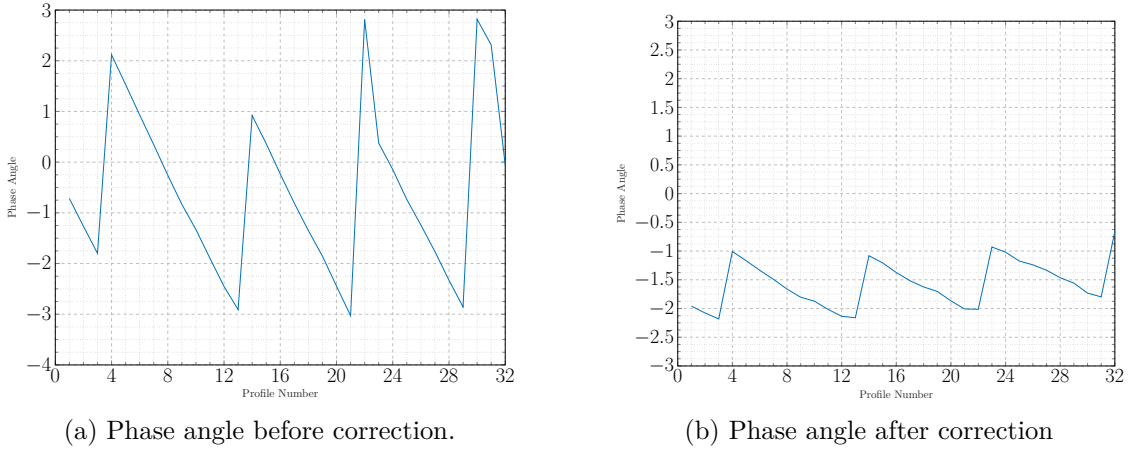


Figure 4.27: Reference HRR profile selected for use in MDSAF using Correlation range-aligned simulated HRRPs.

Figure 4.27 shows that the profile with the highest collective DS power was the selected reference profile. Therefore, the reference profile selection was implemented correctly.



(a) Phase angle before correction.

(b) Phase angle after correction

Figure 4.28: First DS's phase angle before and after MDSAF phase correction.

Furthermore, Figure 4.28 shows the phase of one of the eleven selected DSs before and after phase correction. Figure 4.28b shows that the angle was reduced after phase correction but was not zero. A similar result was seen for all DSs. As discussed in [8], algorithm 4 does not expect the phase to be removed but rather to be reduced. Therefore, since the angles of all the DSs were smaller after phase correction, the phase correction in lines 25-28 in algorithm 4 was implemented correctly.

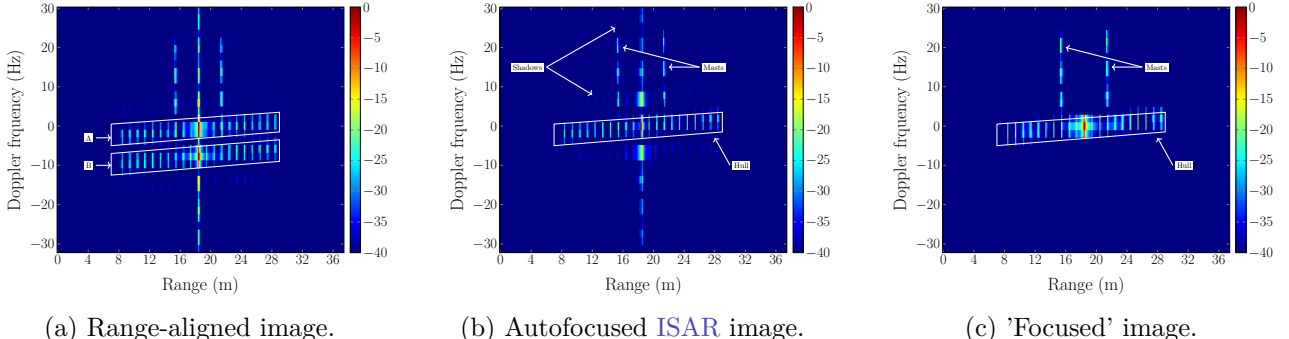


Figure 4.29: (a) Correlation range-aligned ISAR image, (b) MDSAF autofocused ISAR image, (c) ISAR image of simulated object with 0 m/s translation motion.

The scatterer coordinates in Figure 4.1a illustrate that the simulated ship consisted of a single, thin hull and two masts. However, in Figure 4.29a, there are two prominent groups of scatterers, labelled A and B, giving the false impression of two hull-like features on the simulated object. The duplication of the hull in Figure 4.29a was caused by phase errors in the HRRPs. To address this, MDSAF was applied to the Correlation range-aligned profiles.

Figure 4.29b shows a single prominent group of scatterers centered at zero-Doppler which correctly represents the hull. The missing duplication of the hull shows that the image was more focused after applying MDSAF. To quantitatively analyse the focus of the image, the IC was calculated. Before AF the IC was **24.73** and after AF it was **38.42**. The improvement of the IC after MDSAF further confirms that the image focus improved. Therefore, algorithm 4 was implemented correctly.

While the implementation was correct, comparing Figure 4.29b to Figure 4.29c shows that the hull of the ship remained defocused after AF. In Figure 4.29b the ship's hull and masts appear to have faint scatterer sidelobes which indicate that MDSAF did not perfectly correct the scatterer phases. This is attributed to the use of misaligned HRRPs. Nevertheless, the image was more focused after RA and MDSAF was implemented correctly.

4.6.3 Algorithm Validation

In this subsection, measured Correlation range-aligned HRRPs were used to validate that algorithm 4 produced a focused ISAR image.

In algorithm 4, 11 DSs are selected, however it was found that not all HRRPs contained enough DSs to fulfill this requirement. In these cases, the number of DSs was chosen as the maximum number possible. To this effect, the implementation was improved as shown in Listing 4.3.

```

1 if(size(candidate_scatterers_idx,2)>11)
2     num_scatterers = 11;
3 else % use maximum number of scatterers available
4     num_scatterers = size(candidate_scatterers_idx,2);
5 end

```

Listing 4.3: MATLAB code for selecting number of DSs.

Additionally, it was found that scatterers outside the object were chosen as candidate DSs. The aim of AF is to focus the object within the image. Selecting scatterers that do not appear on the object can result in degradation of the focus of the image. Scatterers that appear outside of the object are referred to as noisy scatterers. An improvement was made to the implemented algorithm to ensure that only object scatterers were considered for candidate DS selection. This was implemented as a filtering technique; first scatterers above the average power were found and then the minimum and maximum values were used find the range of scatterers that represented the image. The implementation is shown in Listing 4.4.

```

1 no_noise_scatterers_idx = find(amplitude_mean>0.5.*mean(amplitude_mean));
2 no_noise_scatterers_idx = min(no_noise_scatterers_idx):max(no_noise_scatterers_idx);

```

Listing 4.4: MATLAB code for filtering scatterers used in candidate DS selection.

Figure 4.30 shows the noise filtering threshold introduced and that scatterers 31 to 72 are considered to be within the object.

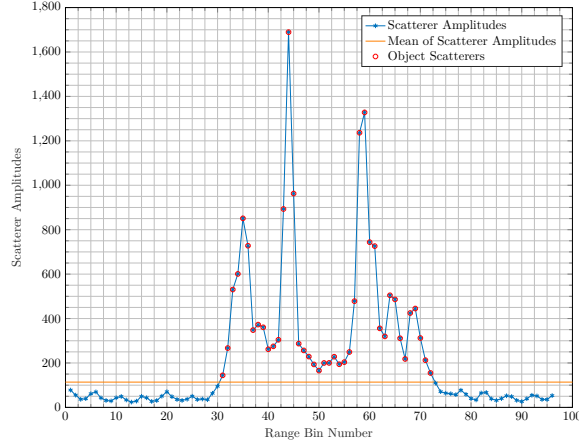


Figure 4.30: Scatterer Amplitudes and object scatterers considered in MDSAF of Correlation range-aligned measured HRRPs.

Figure 4.31a shows the candidate DSs selected before noise filtering was applied. Candidate scatterers outside of the object range of 31 to 72 were erroneously considered and selected as DSs. Figure 4.31b shows the candidate DSs selected after noise filtering was applied. Only scatterers within the object were considered as candidates and selected as DSs. This indicates that the noise filtering was successful.

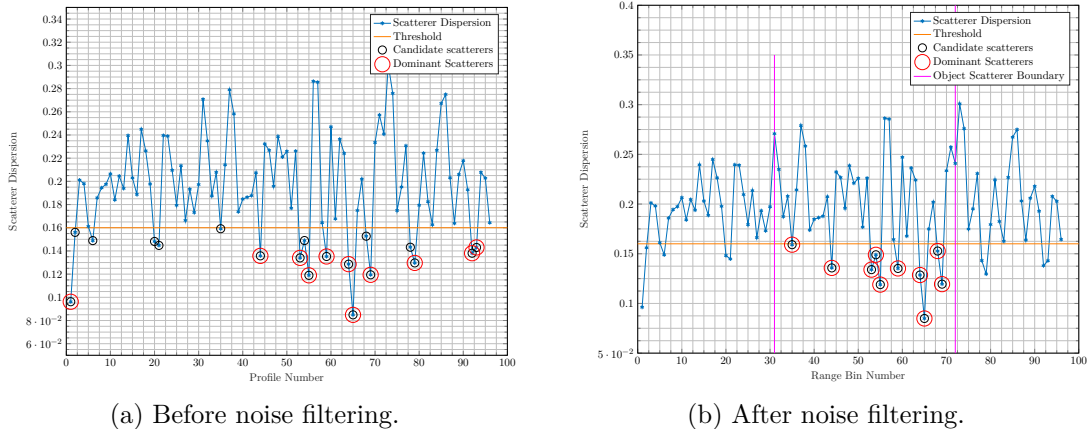


Figure 4.31: MDSAF DS selection for Correlation range-aligned measured HRRPs before and after noise filtering.

The selected DSs shown in Figure 4.31b were used to correct the phase errors introduced by RA.

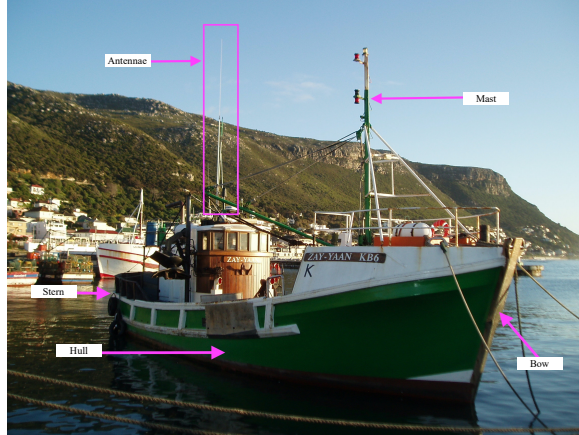


Figure 4.32: Optical image of Zay-Yaan KB6 fishing boat. Adapted from [1].

Figure 4.33a shows the unfocused ISAR image. Comparing it to the image of the Figure 4.32, the mast and antennae features were poorly represented in the ISAR image. Applying RA, resulted in reduced range spreading and so the ISAR image in Figure 4.33b more accurately represented the boat's features; a thin long rectangular cluster of scatterers clearly shows the antennae and the angular bow of the boat is well reflected. However, this image still exhibited Doppler spreading and sidelobes which could be improved by AF.

Figure 4.33c exhibits reduced spreading in the Doppler axis which was attributed to the phase correction performed during MDSAF. Additionally, the rectangular group of antennae and triangular shape of the mast better represent the features in Figure 4.32. Thus the image was visually more focused after MDSAF.

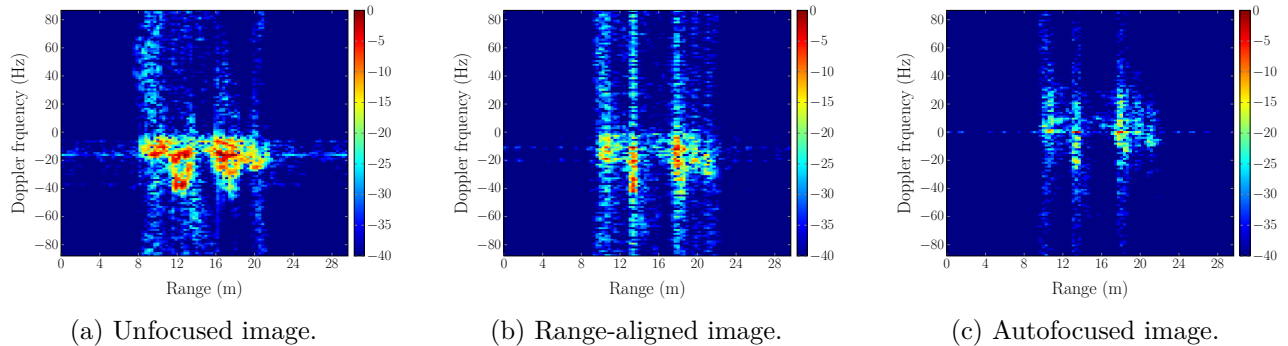


Figure 4.33: ISAR images formed using the original, Correlation range-aligned and MDSAF autofocused HRRPs of a single measured data frame.

Additionally, the IC values were used to quantitatively examine the improvement of image focus. The IC values were **7.0534**, **8.1803** and **17.0869** for the images in Figure 4.33(a),(b) and (c), respectively. The IC improvement factor after RA and AF was calculated to be $\frac{17.0869 - 8.1803}{8.1803} = 108.88\%$ which further indicated that the MDSAF improved the focus of the ISAR image.

Importantly, the focused image in Figure 4.33c still exhibited Doppler spreading but it was significantly reduced compare to the unfocused and range-aligned images. Therefore, the improved implementation of the MDSAF algorithm produced a more focused image of measured data and was validated for use in this report.

4.7 Optimisation of Implementation to Reduce Runtime

The algorithms implemented in this chapter are investigated for use in a QLP. To decrease the runtime of the processor, the algorithm implementations were optimized.

MATLAB is designed to operate on arrays and matrices and has built-in functions that enable multi-threaded processing of matrix operations. This eliminates the need for iterative loops required in other programming languages. The implementation of all algorithms used in this report leveraged these capabilities to achieve improved runtime performance. Additionally, *find()* was replaced with MATLAB logical indexing [24] where possible. All optimisation changes and adjustments were carefully checked to ensure that the same results were produced.

4.7.1 Correlation RA Algorithm

Cross-correlation can be performed in the time or frequency domain, [2] states that the frequency domain computation is faster. However, MATLAB has a built-in two-dimensional time domain cross-correlation function that is optimised for MATLAB use. This made the time domain calculation faster than performing multiple steps to do the frequency domain correlation in this MATLAB specific implementation.

4.7.2 Haywood RA Algorithm

The initial implementation was revised for further optimisation. This process involved introducing global parameters to reduce the frequency of function calls. In the initial version, the correlation RA algorithm was used to perform cross-correlation, while in the revised script, this operation was directly integrated into the code. This revision not only reduced runtime but also removed the dependence on another algorithm.

4.7.3 SDSAF Algorithm

Further optimisation was achieved by introducing global parameters to reduce the frequency of function calls. While this adjustment required the code to be restructured, it still yielded the same results.

4.7.4 MDSAF Algorithm

The MATLAB functions used to calculate values in the algorithm were optimized to use faster alternatives that still yielded the correct results. For example, the *mink()* function, which returns the index of the smallest k values, was replaced by the *sort()* function, and the returned array was then indexed. This change was made because *sort()* is multithreaded, and resulted in runtime improvements.

4.7.5 Runtime Testing

To ensure that the changes made to each algorithm resulted in runtime improvements, the algorithms before and after optimisation were timed.

Testing Setup

A MATLAB [timing script](#) was used to measure the runtime of each algorithm, before and after optimisation. This script was used to execute each algorithm 100 times and the raw timing results were recorded in a CSV file. The timing tests were performed on a single simulated [ISAR](#) frame, which had 32 profiles, each with 256 range bins. A folder containing the testing files is available on [GitHub](#).

The testing was conducted on a MacBook Pro (2016) with the following hardware specifications:

- Processor: 2.9 GHz Dual-Core Intel Core i5
- Memory: 8 GB 2133 MHz LPDDR3

Results

The raw timing results recorded in the CSV file were averaged to determine the effective runtime of each algorithm. [Table 4.2](#) contains the effective runtime of each algorithm before and after runtime optimisation. The runtime improvement was calculated as

$$\text{Improvement} = \frac{\text{Original} - \text{Optimised}}{\text{Original}} \quad (4.1)$$

and is recorded in [Table 4.2](#).

Algorithm	Original Runtime (s)	Optimised Runtime (s)	Improvement (%)
Correlation RA	0.009556872	0.002843406	70.24
Haywood RA	0.011963056	0.004136744	65.42
SDSAF	0.002407375	0.001363729	43.35
MDSAF	0.002260847	0.001801478	20.31

Table 4.2: Algorithm runtime optimisation timing results.

The results recorded in [4.2](#) show that for all algorithms the optimisation strategies resulted in improved runtimes.

4.8 Summary

- The integer bin shifting limitation of the Correlation RA algorithm prevented perfect alignment of the HRRPs when simulated data was used. This was the expected result as seen in the literature [11]. Unexpectedly, when using measured data the profiles were range-aligned. This was likely an anomaly and may not be observed when using other frames of measured data.
- The Haywood RA realised fractional bin shifts and produced range-aligned profiles in both simulated and measured data.
- In measured data, there was often more than one DS. A limitation of the SDSAFA was that it used only one DS to focus the ISAR image. This limited how well the image could be focused when using measured data. A SF was introduced to ensure a high-power DS was selected. This

subsequently improved the performance of the algorithm. [SDSAF](#) produced satisfactorily focused images for measured data.

- [MDSAF](#) realised the use of multiple [DS](#)s to focus the image. The algorithm's performance was improved by adding noise filtering and a systematic way of selecting the reference profile. [MDSAF](#) produced focused images for measured data.
- The processing time of all algorithms was successfully reduced through optimisation of the implementations.

Chapter 5

Quick-look Processor: Design

This chapter describes the design process and approach followed to implement a [QLP](#) for [ISAR](#) imaging of sea vessels. First, the technical requirements were defined and the measured data used during development was described. Thereafter, the algorithms verified and validated in [chapter 4](#) were used to develop four candidate [QLP](#) designs. The measured dataset was used to evaluate each design in terms of the technical requirements. Finally, the [QLP](#) was implemented as a MATLAB app.

5.1 Technical Requirements

The following technical requirements were determined using the report objectives discussed in [chapter 1](#).

Number	Description
TR01	The QLP should process the data in a shorter time than the measurement time of the data.
TR02	The QLP should produce a more focused ISAR image after motion compensation.
TR03	The QLP should be user-friendly.

Table 5.1: Technical requirements considered when designing the [QLP](#).

5.2 Measured Dataset

A dataset with data recorded of a Zay-yaan fishing boat was obtained from the [CSIR](#). The dataset contained 4473 [HRRPs](#), each with 96 range bins. The boat was moving towards the radar throughout the entire measurement interval. Parameters of the [SFW](#) used to capture the data are given in [Table 5.2](#). A picture of the Zay-yaan boat is shown in [Figure 4.4](#).

Parameter	Value
Center Frequency (f_0)	8.51 GHz
Frequency Step (Δf)	5 MHz
Pulse Repetition Interval	0.0057 s

Table 5.2: [SFW](#) parameters of measured dataset used in [QLP](#) design.

5.3 Design Implementation

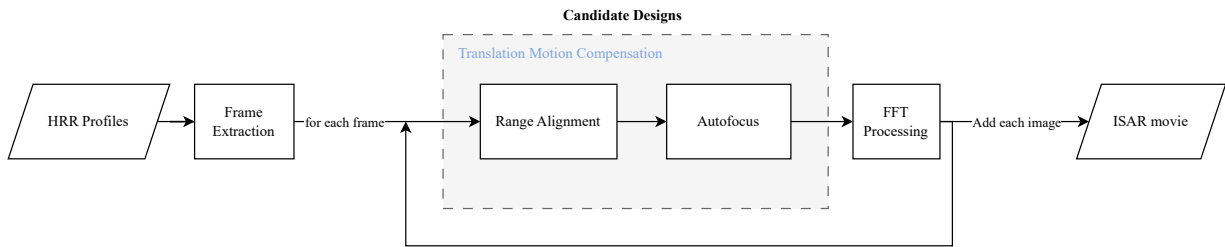


Figure 5.1: Block diagram showing initial QLP design.

5.3.1 Frame Extraction

As discussed in [2], an object's motion relative to the radar over a period in time provides HRR data that can be used to form an ISAR image. Sea vessels have complex motion that often changes drastically over time and leads to defocused ISAR images as discussed in chapter 2.

The measured data contained many range profiles which were gathered over a time period of approximately 25 s. To ensure focused ISAR images were achieved, the range profiles were broken up into subsets called frames. Each frame was used to produce a single ISAR image of the boat.

Two important values were used to create the frames; **CPI** and frame overlap. For the purpose of this report, the **CPI** was kept constant at 128 **HRRPs** for all investigations. However, it should be a user-configurable parameter. Additionally, the frame overlap was calculated as

$$\text{frame overlap} = \text{overlap} \cdot CPI \quad (5.1)$$

where overlap is a value between 0 and 1. A constant overlap of 0.5 was used throughout this report however, in addition to the [CPI](#), it should be user configurable.

Using these values, the number of frames in the dataset was calculated as

$$number\text{ }of\text{ }frames = \lfloor \frac{1 + number\text{ }of\text{ }profiles - CPI}{CPI - profile\text{ }overlap} \rfloor \quad (5.2)$$

where the number of profiles is the number of HRRPs in the dataset and $\lfloor \cdot \rfloor$ is the floor function.

5.3.2 Candidate Designs

The RA and AF algorithms that were validated and verified in chapter 4 were considered for use in the final QLP. The four candidate designs are listed in Table 5.3.

Candidate Design	RA Algorithm	AF Algorithm
1	Correlation	Single Dominant Scatterer
2	Correlation	Multiple Dominant Scatterer
3	Haywood	Single Dominant Scatterer
4	Haywood	Multiple Dominant Scatterer

Table 5.3: Description of candidate QLP designs.

To determine the most suitable candidate design, all designs were validated against the technical requirements in [Table 5.1](#).

5.4 Runtime Testing

In this section, the runtime performance of each candidate design listed in [Table 5.3](#) was assessed to determine which designs met TR01: the [QLP](#) should process the data in less time than the measurement time of the data. To achieve this, the data loading, [TMC](#) processing, and video generation time was included in the overall runtime assessment. This approach ensured that runtime expectations of the [QLP](#) were not distorted by only considering the [TMC](#) processing time.

5.4.1 Experimental Setup

A MATLAB [timing script](#) was used to measure the runtime of each candidate [QLP](#) design. The script was used to run each candidate design 100 times and the raw timing results were recorded in a CSV file. The timing tests were performed using a single measured dataset. A folder containing the testing files is available on [GitHub](#).

The testing was conducted on a MacBook Pro (2016) with the following hardware specifications:

- Processor: 2.9 GHz Dual-Core Intel Core i5
- Memory: 8 GB 2133 MHz LPDDR3

5.4.2 Results and Discussion

The raw timing results recorded in the [CSV file](#) were averaged to determine the effective runtime of each candidate design. The effective runtimes are shown in [Table 5.4](#).

Candidate Design	Runtime (s)
1	21.1222
2	21.1687
3	21.1435
4	21.2206

Table 5.4: Effective runtimes of each candidate [QLP](#) design for a single measured dataset.

The measurement time of the dataset used for time testing was 25.4138 s. To meet TR01 in [Table 5.1](#), the [QLP](#) needed to process the dataset in less than 25.4138 s. The results presented in [Table 5.4](#) show that all candidate designs had runtimes of less than 25.4138 s. While there were variations in the speed of these designs, the difference between the fastest and slowest design was 0.0984 s. This shows that the differences in speed between designs were marginal. Therefore, all candidate designs met TR01 and, based solely on their runtimes, were suitable for use in the final [QLP](#).

5.5 Image Focus Testing

In this section, tests were conducted to assess which candidate designs fulfilled TR02: the QLP should produce a more focused ISAR image after motion compensation.

5.5.1 Experimental Setup

A MATLAB testing script was used to process the measured data using each of the candidate designs. The four measured data frames discussed in section 4.2, which all show a clear side-view of the boat, were used. The unfocused ISAR images formed from these frames are shown in Figure 5.2.

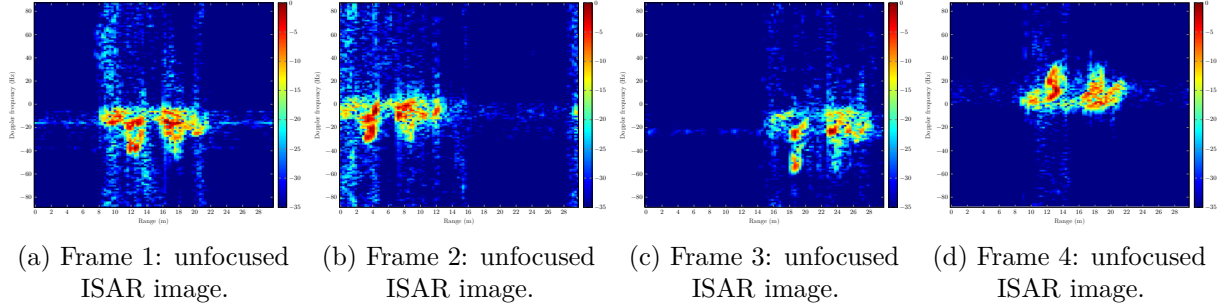


Figure 5.2: Different ISAR image frames produced from a single measured dataset, before TMC was applied.

The IC values before and after TMC were recorded and the ISAR images were generated.

5.5.2 Results and Discussion

The IC values before and after TMC, for each candidate design and frame, were recorded in Table B.1. The IC improvement achieved by each candidate design was calculated as

$$\text{Improvement} = \frac{\text{Unfocused IC} - \text{Focused IC}}{\text{Unfocused IC}} \quad (5.3)$$

where Focused IC was the IC value of the ISAR image produced by each candidate design. The values in Table B.1 were used to calculate the values in Table 5.5.

Frame	IC Improvement (%)			
	Design 1	Design 2	Design 3	Design 4
1	47.92	142.3	69.32	103.4
2	0.4283	12.53	17.13	66.16
3	5.170	26.45	13.58	35.82
4	28.99	75.68	62.44	80.98

Table 5.5: The IC improvement of the ISAR image produced by each candidate QLP design compared to the IC of the unfocused image for multiple frames of measured data.

Frame 1

The IC improvement values in Table 5.5 indicated that candidate design 2 produced the image with the most improved focus. However, comparing all 4 images in Figure 5.3, visually, design 3 and 4 produced

a more focused image than design 2. This was evident by the reduced spreading of scatterers in the Doppler axis. However comparing the range spreading of the images in Figure 5.3d and Figure 5.3c, design 3 displayed less range spreading. Therefore it was the best focused. Figure 5.3b exhibits significant Doppler spreading despite it having the greatest IC improvement. This indicated that the IC value was not always an accurate representation of the image focus.

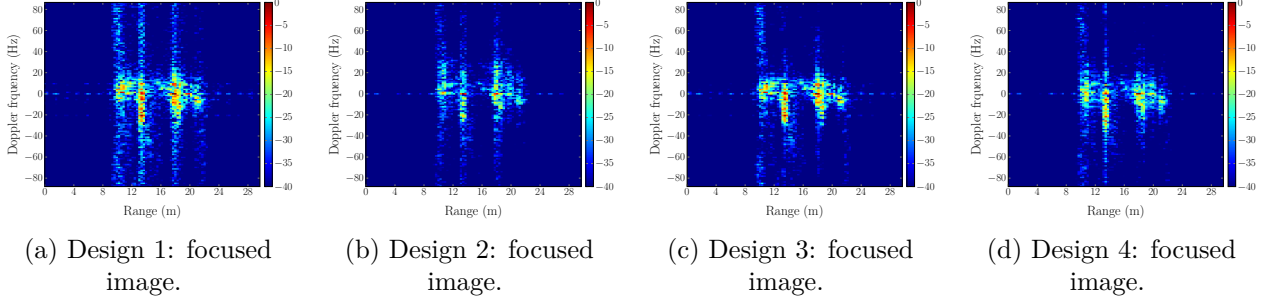


Figure 5.3: ISAR images produced by each candidate design for frame 1 of the measured dataset.

Frame 2

The IC improvement values recorded in Table 5.5 indicated that candidate design 4 produced the image with the most improved focus. Design 4 produced Figure 5.4d which has significantly less Doppler spreading than the ISAR images produced by the other designs in Figure 5.4. Additionally, it displayed the least range spreading. Since design 4 was able to produce a well-focused image, the poor focus in the other images was not attributed to the data but rather the performance of the algorithms used.

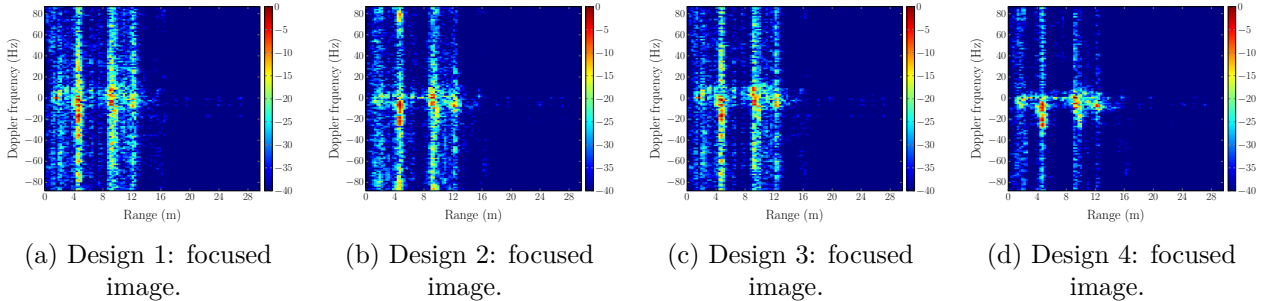


Figure 5.4: ISAR images produced by each candidate design for frame 2 of the measured dataset.

Frames 3 and 4

The IC values again indicated that candidate design 4 improved the focus of the ISAR images of frames 3 and 4 the most. Comparing the images in Figure 5.5, the boat's features were spread over the Doppler axis in (a) and (c), but in (b) and (d) there was less spreading. There was less Doppler and range spreading in (d) than in (b), therefore it was more focused which was in agreement with the IC values in Table 5.5.

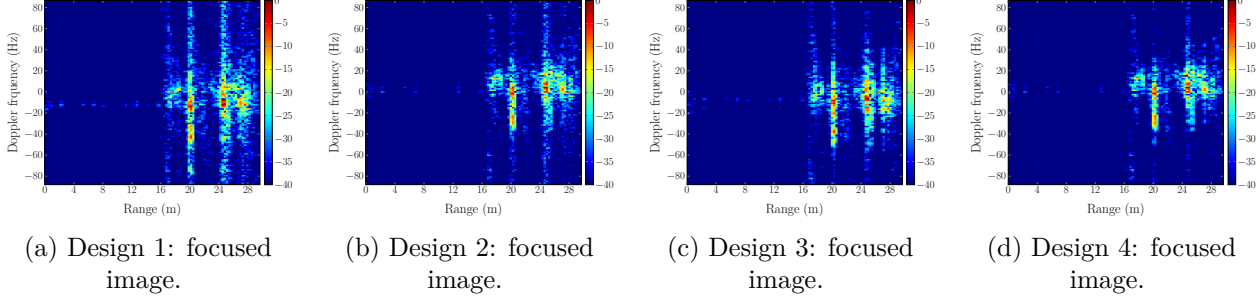


Figure 5.5: ISAR images produced by each candidate design for frame 3 of the measured dataset.

The IC improvement values for frame 4 indicated that design 4 produced the most focused image. Comparing the images in Figure 5.6, further confirmed this. Figure 5.6d produced the image with least Doppler and range spreading (best seen by comparing the mast in each image). Whilst Figure 5.6c looks similarly well focused, there is more range spreading which can be seen in the poor representation of the triangular shape of the mast which can be clearly seen in Figure 5.6d.

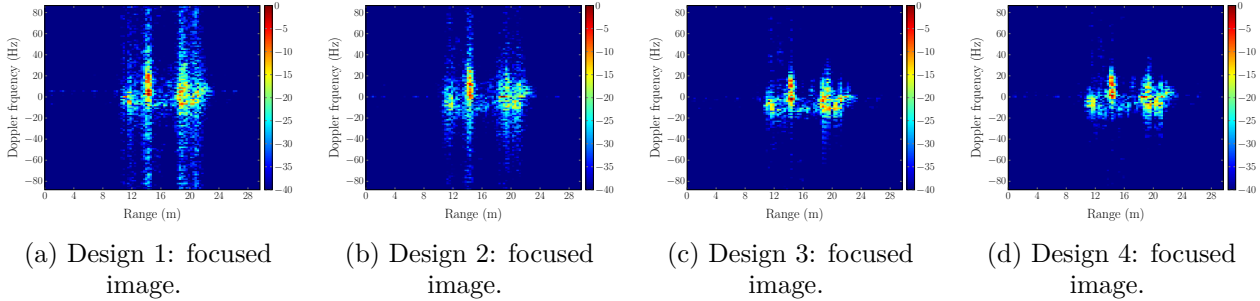


Figure 5.6: ISAR images produced by each candidate design for frame 4 of the measured dataset.

5.6 Summary of Findings

It was found that all four candidate designs met the timing requirement, TR01. The design with the fastest runtime was candidate design 2, Haywood RA and SDSAF. However it was only 0.1 s faster than the slowest design, candidate design 4. Consequently, the performance of each candidate design when focusing multiple measured data frames was the deciding factor for choosing the final design for implementation.

In all of the frames, candidate design 4 consistently performed well. Although, candidate designs 2 and 3 performed well when focusing some frames, they did not perform well for others. Candidate design 1 did not perform well in any frames.

Therefore, since candidate design 4 met both TR01 and TR02, it was selected for the final QLP design implemented in this report.

Additionally, candidate design 4 produced multiple focused ISAR image frames from the same dataset.

It then followed that the final **QLP** was inherently able to produce focused **ISAR** images from valid measured **HRRPs**. As discussed in [chapter 2](#), some data is not conducive to forming a focused **ISAR** image, regardless of the **TMC** algorithms applied. Therefore, there might exist cases where the **QLP** does not produce focused images of the object because of the data used.

5.7 Final Design

[Figure 5.1](#) was updated to reflect the final design and is shown in [Figure 5.7](#).

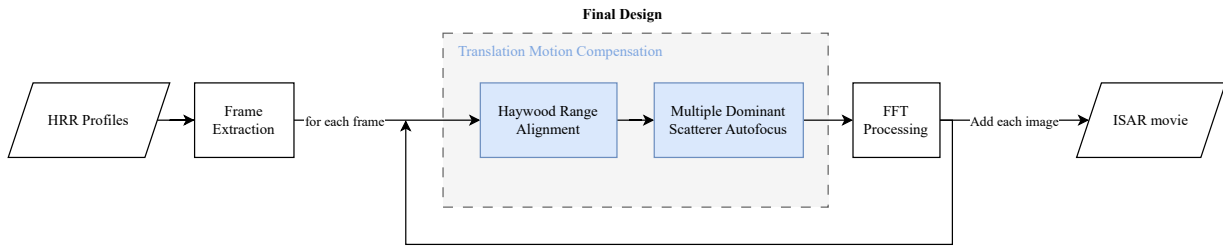


Figure 5.7: Block diagram showing the final **QLP** design.

This final **QLP** design was initially implemented as MATLAB [script](#). It enabled users to configure the **CPI** and overlap parameters for frame extraction. However, the effects of these values on the focus of **ISAR** images was not investigated in this report.

To meet TR03, user-friendly design, a MATLAB app was designed. The remainder of this section gives an overview of the functionality of the app.

5.7.1 App design

The app was designed to be simplistic in nature, with minimal features to aid in usability. The packaged MATLAB app can be [downloaded](#) and installed to the MATLAB tool strip for use. Initially, a wireframe of the basic app design was created and is shown in [Figure 5.8](#). Although **CPI** and frame overlap were kept constant in this report, they were considered to be a useful parameters and were added as user inputs in the app. Additionally, playback control settings were added to allow users to pause the video and control playback speed.

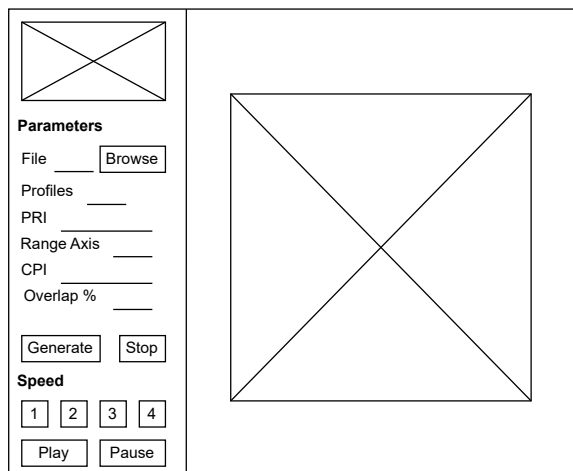


Figure 5.8: Wireframe of **QLP** MATLAB app.

Using the wireframe, the UI was designed in MATLAB. Figure 5.9 shows how the app responded to user interactions and Table 5.6 describes the functionality in more detail.

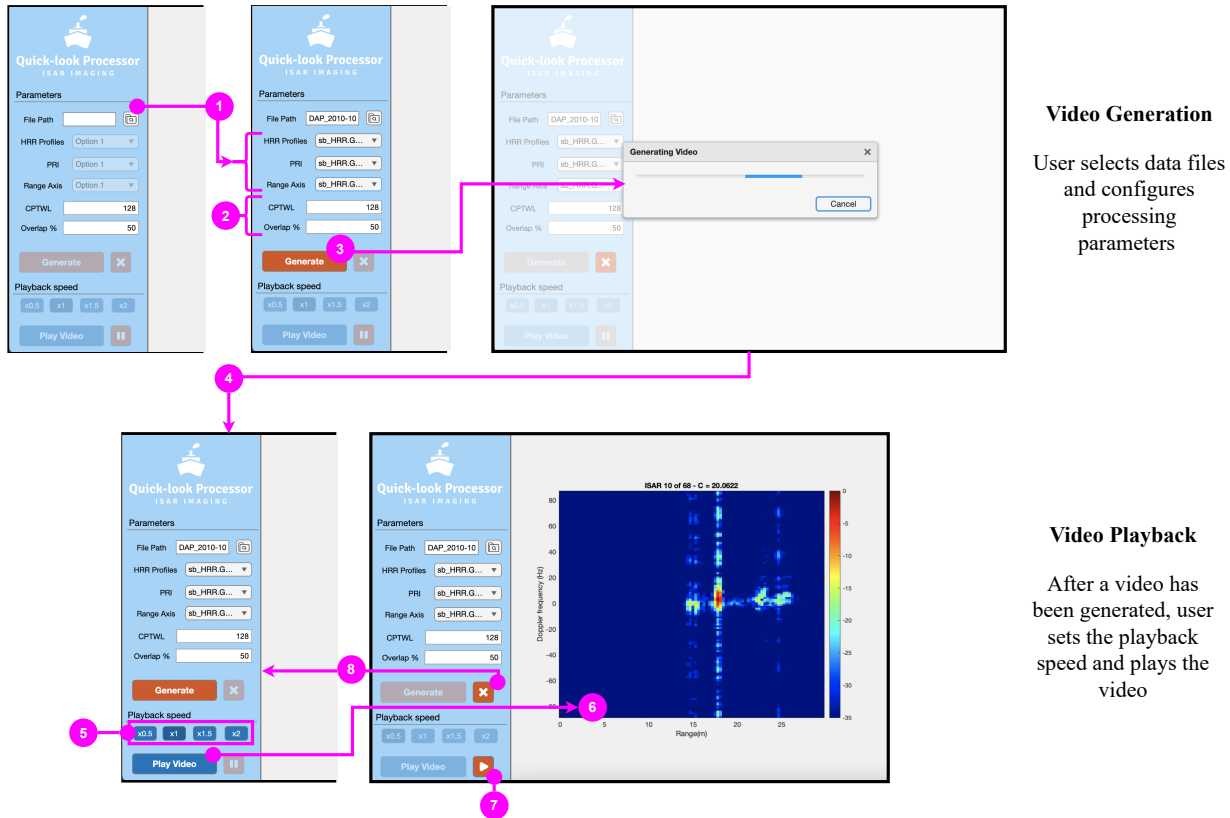


Figure 5.9: User flow diagram using the designed UI of the QLP MATLAB app.

The user interactions labeled in Figure 5.9 were described in more detail in Table 5.6

Number	Description
1	Choose a MATLAB structure with HRR profile data on the host device. If selected, the HRR , PRI , and Range Axis dropdown lists will auto-populate with available fields for selection. Values must be assigned to all three fields to enable the <i>Generate</i> button.
2	The CPI and Overlap % values are set to 128 and 50 by default. These can be changed if desired.
3	When <i>Generate</i> is clicked, a loading screen appears whilst the ISAR video is generated in the background.
4	After generation is complete, the video is saved to the host device as ISARmovie.mj2, and the video playback settings are then enabled.
5	The Playback speed buttons can be used to control the speed of the video and should be set before clicking <i>Play Video</i> .
6	When <i>Play Video</i> is clicked, the generated video is played at the selected speed in the right-hand panel.
7	Pause/Play video button
8	Clicking ‘Cancel’ will stop the playback. The last played frame will still be visible and the <i>Generate</i> button will become enable.

Table 5.6: Description of user interactions and **QLP** app flow.

Chapter 6

Quick-look Processor: Case Studies

This chapter aimed to show how the [QLP](#) could be used to assess the quality of recorded data during field trials. The [QLP](#) was designed to generate focused [ISAR](#) images from measured [HRRPs](#) of sea vessels. In the design phase, it was established that the [QLP](#) could produce multiple focused image frames from a dataset.

This chapter focuses on the application of the [QLP](#) in real-world scenarios. Specifically, case studies are employed to evaluate the [QLP](#)'s efficiency and its utility in data quality assessment. All datasets used in these case studies were collected by the [CSIR](#), and permission was obtained to use them.

6.1 Case Study 1: Impact of [HRR](#) Profiles and Range Bins on [QLP](#) Runtime

This case study was used to investigate how the number of [HRRPs](#) and range bins in a dataset affected the runtime of the [QLP](#). The runtime included the data transfer and [TMC](#) processing times.

6.1.1 Setup

The testing was conducted on a MacBook Pro (2016) with the following hardware specifications:

- Processor: 2.9 GHz Dual-Core Intel Core i5
- Memory: 8 GB 2133 MHz LPDDR3

For each test, a [timing script](#) was used to run the dataset through the [QLP](#) 100 times and the raw timing results were recorded in a CSV file. The [CPI](#) and frame overlap percentage were 128 [HRRPs](#) and 50 %, respectively.

Test 1: Varying number of [HRR](#) Profiles

A single dataset containing 96 range bins was broken into subsets, each with a different number of profiles. These subsets were each run through the [QLP](#).

Test 2: Varying number of Range bins

Three datasets with varying numbers of range bins (69, 86, and 96) were used. Each dataset was subsetted to ensure a consistent count of 2091 [HRRPs](#) was used.

6.1.2 Results and Discussion

The raw timing results collated in a single CSV file (`timing_profiles.csv` and `timing_bins.csv`) for each respective test were averaged to determine the effective **QLP** runtime for each test case.

The effective runtimes for the varying number of profiles are shown in ??.

Subset Number	HRR Profiles	Measurement Time (s)	QLP Runtime (s)
1	497	2.8238	3.0893
2	1491	8.4713	7.9452
3	4473	25.4138	21.8972

Table 6.1: Effective **QLP** runtimes for datasets that had different a number of **HRRPs** but the same number of range bins.

For subset 1 in Table 6.1, where the number of profiles was small, the runtime exceeded the data measurement time by 0.2655 s. This was attributed to the inclusion of data transfer time in the **QLP** runtime. However, as the number of profiles increased, the runtime was observed to be less than the measurement time.

Therefore it was shown that, as the number of profiles increased, the **QLP** became more efficient. Consequently, for a smaller number of profiles, depending on hardware specifications, the **QLP** runtime may exceed the measurement time due to data transfer overheads. However, the runtime exceeds the measurement time by less than 1 s, therefore the **QLP** remains suitable for use in field testing.

Table 6.2 shows the effective **QLP** runtimes when the number of range bins was varied. For all three datasets, the **QLP** runtime was less than the measurement time, as expected. Interestingly, as the number of range bins changed, the **QLP** runtime only varied within 1 s. This differed to the results observed when the number of profiles was varied. Hence, the number of profiles was a more significant contributor to the **QLP** runtime.

Dataset Number	Range Bins	Measurement Time (s)	QLP Runtime (s)
1	69	17.7785	10.2486
2	86	16.8664	10.5936
3	96	11.8802	10.4670

Table 6.2: Effective **QLP** runtimes for datasets that had different a number of range bins but the same number of **HRRPs**.

Overall, the **QLP** runtime became more efficient as the dataset size increased. This is desirable as field tests are likely to use datasets upwards of 20 s

6.2 Case Study 2: Using **QLP** to Visualise **ISAR** Images for Data Quality Assessment

As discussed in [6], a focused **ISAR** image does not necessarily have a high Doppler resolution. The quality of the recorded data affects the range and Doppler resolution of the **ISAR** image. Furthermore,

6.2. Case Study 2: Using QLP to Visualise ISAR Images for Data Quality Assessment

the quality of the recorded data is impacted by the recording setup and other environmental conditions [5].

As validated in chapter 5, the QLP successfully generated focused ISAR images using a measured dataset. This case study was conducted to show how the QLP could be used to assess the quality of data collected for ISAR imaging. This subsequently gave feedback on whether the data collection setup was conducive to producing desireable ISAR images of the object. Different datasets which recorded the same Zay-yaan boat, but were collected using different SFW parameters were used.

6.2.1 Setup

Two datasets, collected by the CSIR [1], were used in this case study. Both datasets contained HRRPs of a *Zay-yaan KB6* fishing boat. The first dataset was the same dataset used to design the QLP in chapter 5. The second dataset was collected using different wave parameters to the other two datasets. The SFW parameters of the respective datasets are given in Table 6.3.

Parameter	Values	
	Dataset 1	Dataset 2
Center Frequency (f_0)	8.51 GHz	9.82 GHz
Frequency step (Δf)	5 MHz	10 MHz
Pulse Repetition Interval (PRI)	0.0057 s	0.0085 s
Number of HRRPs	4473	2901
Number of bins	96	69

Table 6.3: SFW parameters of two different measured datasets.

Each of these datasets were run through the QLP which produced a video for each dataset. The CPI and frame overlap values were consistently 128 HRRPs and 50 % respectively.

6.2.2 Results and Discussion

The videos produced can be downloaded and viewed offline: zipped videos. These videos were saved as AVI files in an attempt to preserve image quality. The `video_viewer.m` can be used to watch them.

Some frames in the videos were not focused despite the TMC. As discussed in chapter 2, this was an expected result due to the complex motion of the boat and other factors. However, the videos did contain a few focused frames, some of which are shown in ?? and Figure 6.3.

The labelled structure of the *Zay-yaan* boat is shown again in Figure 6.1 for comparison with the ISAR image frames.

6.2. Case Study 2: Using QLP to Visualise ISAR Images for Data Quality Assessment

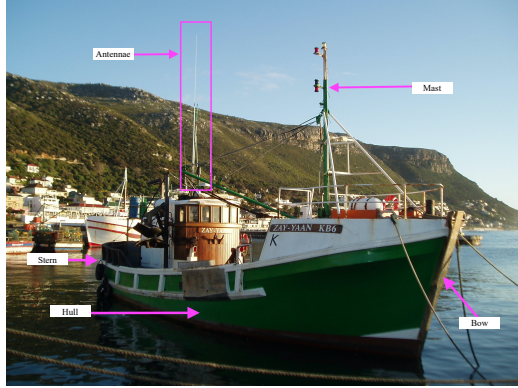


Figure 6.1: Optical image of Zay-Yaan KB6 fishing boat. Adapted from [1].

Figure 6.2 shows three focused frames generated by the QLP using dataset 1. In all three images, the antennae appeared as a long, thin cluster of scatterers that were longer than the mast. Comparing this representation to Figure 6.1, revealed that the antennae were well characterised in the ISAR image frames. Additionally, the hull and rounded shape of the stern were apparent in all frames. The shape of the bow could be seen in both Figure 6.2(a) and (b) but not in (c). In frame 64 (see Figure 6.2c), the bow looked rounded which was not an accurate characterisation of the angular shape seen in Figure 6.1. The mast of the ship was only a clear feature in Figure 6.2b and could not be distinguished from the front of the boat in the other frames. Overall, most features of the boat were accurately represented in the focused ISAR images in Figure 6.2.

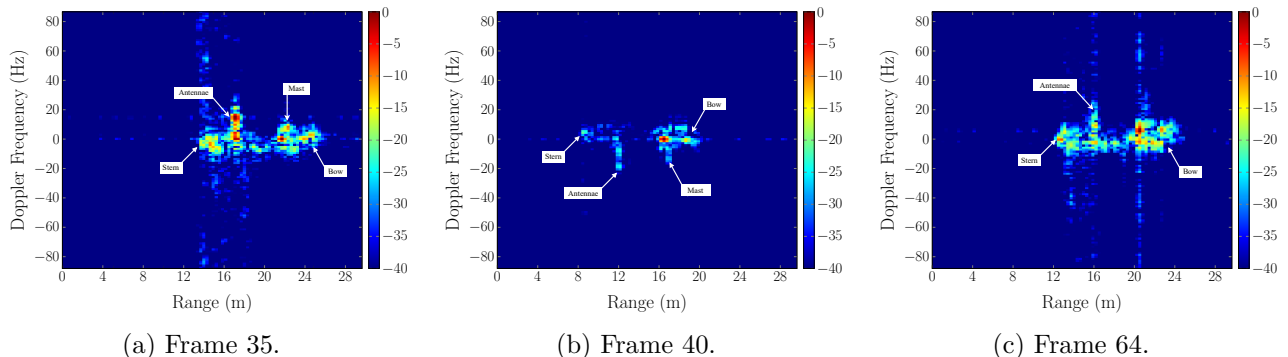


Figure 6.2: Focused ISAR image frames produced by the QLP using dataset 1.

Figure 6.3 shows three focused frames generated by the QLP using dataset 2. Comparing the general shape of the boat in the ISAR images in Figure 6.3 to Figure 6.1, revealed that the ISAR images did not resemble the boat. However, some features such as the stern, bow and cabin were present in the image.

Although these features were identifiable, they are very general features of a boat. This could result in incorrect classification of the object. For example, the elongated hull could result in an incorrect classification of the object as a bulk carrier boat. An optical image of the bulk carrier boat is shown in Figure 3.2a.

6.2. Case Study 2: Using QLP to Visualise ISAR Images for Data Quality Assessment

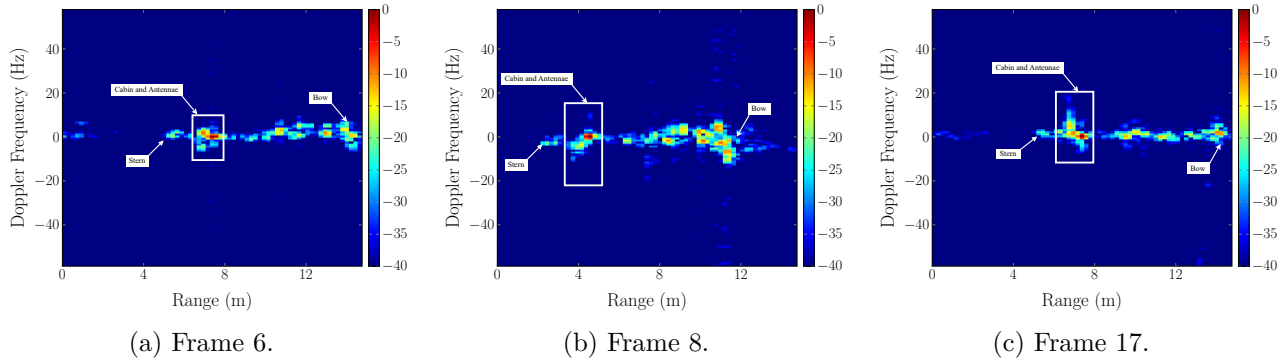


Figure 6.3: Focused ISAR image frames produced by the QLP using dataset 2.

Comparing the frames in Figure 6.2 and 6.3, both sets of images captured general features of a boat that would lead to it being classified as a sea vessel. However, only the images in Figure 6.2 showed a good characterisation of the *Zay-yaan KB6* boat's features. If there has not been prior knowledge of what boat was imaged, the images produced from dataset 1 would have led to correct classification. However, dataset 2 would not likely have been recognised as the *Zay-yaan KB6*.

Furthermore, in both cases the images were focused which revealed that the difference in results was likely caused by the equipment setup. Whilst the SFW parameters used in dataset 1 were suitable to record data that could be used to form high-resolution ISAR images of the boat. However, this was not the case with the parameters used when recording dataset 2.

This comparison demonstrated how the QLP could be used to identify equipment setup errors which resulted in the collection of data that produced undesirable but focused ISAR images. If the QLP had been used in the field when collecting this data, it would have been apparent to the researchers that the setup was unfavourable and corrections could have been made to ensure the collection of good quality data, similar to dataset 1.

It is important to note here that not all frames in the videos are well-focused. These unfocused frames are caused by a variety of factors as discussed in section 3.2

Chapter 7

Conclusions

The main objective of this report was to develop a **QLP** for **ISAR** imaging of sea vessels. The goal was to produce a tool that could be used to assess the quality of data recorded during field experiments. This would prove useful in ensuring that high-quality data is captured, which is invaluable to the continued development of the broader research field.

Following a thorough theoretical background on **ISAR** concepts, a survey of relevant literature was conducted. The survey revealed that most literature discussed the performance of **TMC** algorithms in the context of aircraft, not sea vessels. Moreover, few literature sources comparing these algorithms on a common dataset were found. Next, the survey showed that **QLPs** developed for other radar systems proved to be useful in quality control of recorded data during field experimentation. Although, the literature did not reveal such a system for **ISAR** imaging contexts, systems that produced focused images of large sea vessels in a short duration of time did exist.

An objective of this report was to implement low-computation **TMC** algorithms for the purpose of focusing **ISAR** images of sea vessels. From the literature, two such **RA** and **AF** algorithms were selected and further investigated in [chapter 4](#). Following their implementation in MATLAB, each algorithm was verified using simulated data. Subsequently, a single measured dataset was used to validate their effectiveness in producing focused **ISAR** images of a *Zay-yaan KB6* fishing boat.

During the validation process, deficiencies in the original **SDSAF** and **MDSAF** algorithms were identified. This prompted necessary improvements to enhance their performance in focusing the **ISAR** image. The improved algorithms were validated using the same measured data as before and were found to be more effective. Given that the ultimate goal was to incorporate these **TMC** algorithms into a **QLP**, work was done to optimise the runtime of each algorithm.

This project had the objective of developing a **QLP** that could produce focused **ISAR** images in less time than it took to measure the data. In [chapter 5](#), the **TMC** algorithms were combined to form four candidate **QLPs**. Two tests were developed to evaluate the capability of each candidate design in meeting the technical requirements. First, the runtime of each candidate design when tasked to form multiple **ISAR** images from a single dataset was evaluated. It was found that all candidates performed equally well in processing the data in less time than the data measurement time. The second test assessed each candidate's ability to focus four measured data frames. This test revealed the best candidate design to be a combination of Haywood **RA** and **MDSAF**.

Notably, the investigation into the performance of multiple low-computation **TMC** algorithms on the same measured dataset of a sea vessel addressed a gap in the literature.

After selecting the final **QLP** design, a MATLAB app was designed and developed to improve usability of the **QLP** during field work. To meet the final objective of this report, the app was designed to process datasets containing **HRRPs** and display a video of the generated **ISAR** images. The final app design proved to be a suitable solution to ensuring a user-friendly **QLP** design.

In [chapter 6](#), two case studies were used to show that the **QLP** could be used to assess the quality of measured data during field trials. In the first case study, the **QLP** was shown to efficiently process large datasets in less time than the data measurement time. In the second case study, the **QLP** successfully produced focused **ISAR** images from multiple maritime datasets. A comparison of the images from the two different datasets revealed that that the one dataset's recording setup was not conducive to producing a high-quality image of the boat. This illustrated the **QLP**'s ability to assess data quality.

The report's contents confirm the fulfillment of the project's initial objectives. A **QLP** which generates focused **ISAR** images of sea vessels was designed and developed. Additionally, its runtime efficiency and user-friendly design make it a valuable tool for assessing the quality of recorded data during field experiments.

7.1 Future Work

The time constraints of this project have prevented a holistic investigation into the work discussed in this report. Recommendations for future work on this project are briefly summarised in this chapter.

7.1.1 Algorithms

- Other low computation **TMC** algorithms should be investigated and tested. This could result in a more effective **QLP**.
- The effect of the **CPI** on algorithm performance should be investigated. Research into implementing a low computation time window selection algorithm could prove useful. In this report, the value was kept constant.
- Low computation **RMC** algorithms should be investigated to improve the focus of the images produced, whilst still meeting the timing requirements.
- A wider variety of data should be used to test the algorithms performance to ensure a more robust **QLP**.

7.1.2 Quick-look Processor

- Investigate different candidate designs on different datasets to determine if some designs work better than others in different contexts. The results of this would inform a **QLP** update to allow users to select which algorithms to apply to the measured data.
- Investigate the processor's performance on datasets of objects other than sea vessels to determine its applicability.
- Improve the processor's robustness by facilitating the use of other **ISAR** data types, not only **SFW**.

7.1. Future Work

- The developed MATLAB code could be implemented in a non-licensed programming language like C++ to increase accessibility and possibly performance.
- Improve the functionality of the QLP app by adding additional features and error handling.

Bibliography

- [1] M. Y. Gaffar, W. A. Nel, K. Naicker, J. Steyn, T. Alanazi *et al.*, “Synthetic range profiling, isar imaging of sea vessels and feature extraction, using a multimode radar to classify targets: Initial results from field trials,” *Saudi Int. Electron., Communi. and Photon. Conf. 2011*, Jun. 2011. [Online]. Available: <https://doi.org/10.1109/SIECPC.2011.5876925>
- [2] V. C. Chen and M. Martorella, *Inverse Synthetic Aperture Radar Imaging: Principles, Algorithms and Applications*. SciTech Publishing, 2014.
- [3] M. Y. A. Gaffar, “Ground-based isar imaging of cooperative and non-cooperative sea vessels with 3-d rotational motion,” PhD thesis, University of Cape Town, Dec. 2009. [Online]. Available: <https://open.uct.ac.za/items/947407b1-516a-41ba-a898-e30b5a7666fa>
- [4] C. Özdemir, *Inverse Synthetic Aperture Radar Imaging with MATLAB Algorithms*. John Wiley and Sons, Inc., 2012.
- [5] M. Y. Martin, M. Y. A. Gaffar, and S. L. Winberg, “The development of a quick-look radar processor for detecting small sea vessels,” in *2023 8th Int. Conf. on Signal and Image Process.* IEEE, Jul. 2023, pp. 698–703. [Online]. Available: <https://doi.org/10.1109/ICSIP57908.2023.10270818>
- [6] A. Zyweck, “Preprocessing issues in high resolution radar target classification,” PhD thesis, University of Adelaide, Mar. 1995. [Online]. Available: <https://digital.library.adelaide.edu.au/dspace/handle/2440/18524>
- [7] D. Jordan, M. Inggs, and D. O’Hagan, “Nextlook: A lightweight, real-time quick-look processor for nextrad,” *IET Conf. Publications*, vol. 2017, Oct. 2017. [Online]. Available: <https://doi.org/10.1049/CP.2017.0470>
- [8] C. Yuan and D. Casasent, “Composite filters for inverse synthetic aperture radar classification of small ships,” *Optical Engineering*, vol. 41, no. 1, pp. 94–104, Jan. 2002. [Online]. Available: [10.1117/1.1425789](https://doi.org/10.1117/1.1425789)
- [9] P. J. Archer, “A transputer based implementation of a quick look processor for an airborne sar system,” PhD thesis, University of Cape Town, Jan. 1997. [Online]. Available: <https://open.uct.ac.za/items/ce11e698-8624-4ff7-a0d8-edaa45e35fa7>
- [10] P. of Modern Radar, *Principles of Modern Radar*. SciTech Publishing, 2010.
- [11] V. J. V. Rensburg, A. Mishra, and W. Nel, “High range resolution profile alignment,” Master’s thesis, University of Cape Town, Sep. 2012. [Online]. Available: https://ebe.uct.ac.za/sites/default/files/content_migration/ebe_uct_ac_za/904/files/vjvanrensburg_thesis.pdf
- [12] Wehner and D. R., *High-Resolution Radar*, 2nd ed. Norwood, MA: Artech House, 1995.

- [13] M. Martorella and F. Berizzi, "Time windowing for highly focused isar image reconstruction," *IEEE Trans. on Aerosp. and Electron. Syst.*, vol. 41, no. 3, pp. 992–1007, Jul. 2005. [Online]. Available: <https://doi.org/10.1109/TAES.2005.1541444>
- [14] N. Bon, G. Hajduch, A. Khenchaf, R. Garello, and J.-M. Quellec, "Recent developments in detection, imaging and classification for airborne maritime surveillance," *Signal Process., IET*, vol. 2, pp. 192 – 203, 10 2008. [Online]. Available: <https://doi.org/10.1049/iet-spr:20070082>
- [15] D. Frost and J. R. Tapamo, "Detection and tracking of moving objects in a maritime environment using level set with shape priors," *EURASIP J. on Image and Video Process.*, vol. 2013, pp. 1–16, 12 2013. [Online]. Available: <https://doi.org/10.1186/1687-5281-2013-42>
- [16] J. Wang and D. Kasilingam, "Global range alignment for isar," *IEEE Trans. on Aerosp. and Electron. Sys.*, vol. 39, no. 1, pp. 351–357, Jan. 2003. [Online]. Available: <https://doi.org/10.1109/TAES.2003.1188917>
- [17] J. M. Muñoz-Ferreras and F. Pérez-Martínez, "Subinteger range-bin alignment method for isar imaging of noncooperative targets," *EURASIP J. on Advances in Signal Process. 2010*, vol. 2010, pp. 1–16, May 2010. [Online]. Available: <https://doi.org/10.1155/2010/438615>
- [18] B. Haywood and R. J. Evans, "Motion compensation for isar imaging," in *Proc. Australian Symp. on Signal Process. and Appl.*, R. F. Barrett, Ed., Adelaide, Australia, Apr. 1989, pp. 113–117.
- [19] W. Ye and Z. Bao, "A new autofocus method for inverse synthetic aperture radar: Local dominant scatterer synthesis," *Sci. in China Ser. E: Technological Sci.*, vol. 40, pp. 653–660, Dec. 1997. [Online]. Available: <https://doi.org/10.1007/BF02916851>
- [20] J. Xu, J. Cai, Y. Sun, X.-G. Xia, A. Farina *et al.*, "Efficient isar phase autofocus based on eigenvalue decomposition," *IEEE Geosci. and Remote Sens. Lett.*, vol. 14, no. 12, pp. 2195–2199, Nov. 2017. [Online]. Available: <https://doi.org/10.1109/LGRS.2017.2746758>
- [21] B.-S. Kang, M.-S. Kang, I.-O. Choi, C.-H. Kim, and K.-T. Kim, "Efficient autofocus chain for isar imaging of non-uniformly rotating target," *IEEE Sensors J.*, vol. 17, no. 17, pp. 5466–5478, Jul. 2017. [Online]. Available: <https://doi.org/10.1109/JSEN.2017.2727507>
- [22] M. Aziz, "Isar imaging of non-cooperative sea vessels," 2018. [Online]. Available: https://github.com/MustaqeemAziz/EEE_4022S
- [23] A. Zeke Quezada, "What type of sailboat is this?" Jan. 2023, (accessed Oct. 19 2023). [Online]. Available: <https://asa.com/news/2023/01/09/what-type-of-sailboat-is-this/>
- [24] L. Shure, "Loren on the art of matlab: Logical indexing – multiple conditions," Feb. 2013. [Online]. Available: https://blogs.mathworks.com/loren/2013/02/20/logical-indexing-multiple-conditions/?s_tid=srctitle_support_results_6_logical%20indexing

Appendix A

Repository

All MATLAB scripts used throughout this report, as well as the final MATLAB app can be found at the following link:

<https://github.com/tristynferreiro/QP4ISAR>

The MATLAB package can be downloaded at the following link:

<https://github.com/tristynferreiro/QP4ISAR/app>

Appendix B

Additional QLP Design Results

B.1 Image Contrast values of measured data frames

Table B.1 shows the **IC** values for measured data frames used in the **QLP** design.

Frame	Image Contrast				
	Unfocused	Design 1	Design 2	Design 3	Design 4
1	7.0534	10.434	17.087	11.943	14.349
2	7.284	7.3152	8.197	8.5321	12.103
3	9.3845	9.8697	11.867	10.659	12.746
4	7.739	9.9822	13.596	12.571	14.006

Table B.1: The **IC** values of the **ISAR** image produced by each candidate **QLP** design for multiple frames of measured data.

Appendix C

Ethics Form



PRE-SCREENING QUESTIONNAIRE OUTCOME LETTER

STU-EBE-2023-PSQ000492

2023/07/27

Dear Tristyn Ferreiro,

Your Ethics pre-screening questionnaire (PSQ) has been evaluated by your departmental ethics representative. Based on the information supplied in your PSQ, it has been determined that you do not need to make a full ethics application for the research project in question.

You may proceed with your research project titled:

Quick-look processor for Inverse Synthetic Aperture Radar (ISAR) imaging of sea vessels

Please note that should aspect(s) of your current project change, you should submit a new PSQ in order to determine whether the changed aspects increase the ethical risks of your project. It may be the case that project changes could require a full ethics application and review process.

Regards,

Faculty Research Ethics Committee